

Development of a Synthetic Uterus Model with Embedded Sensing for Multiport Spina Bifida Surgery

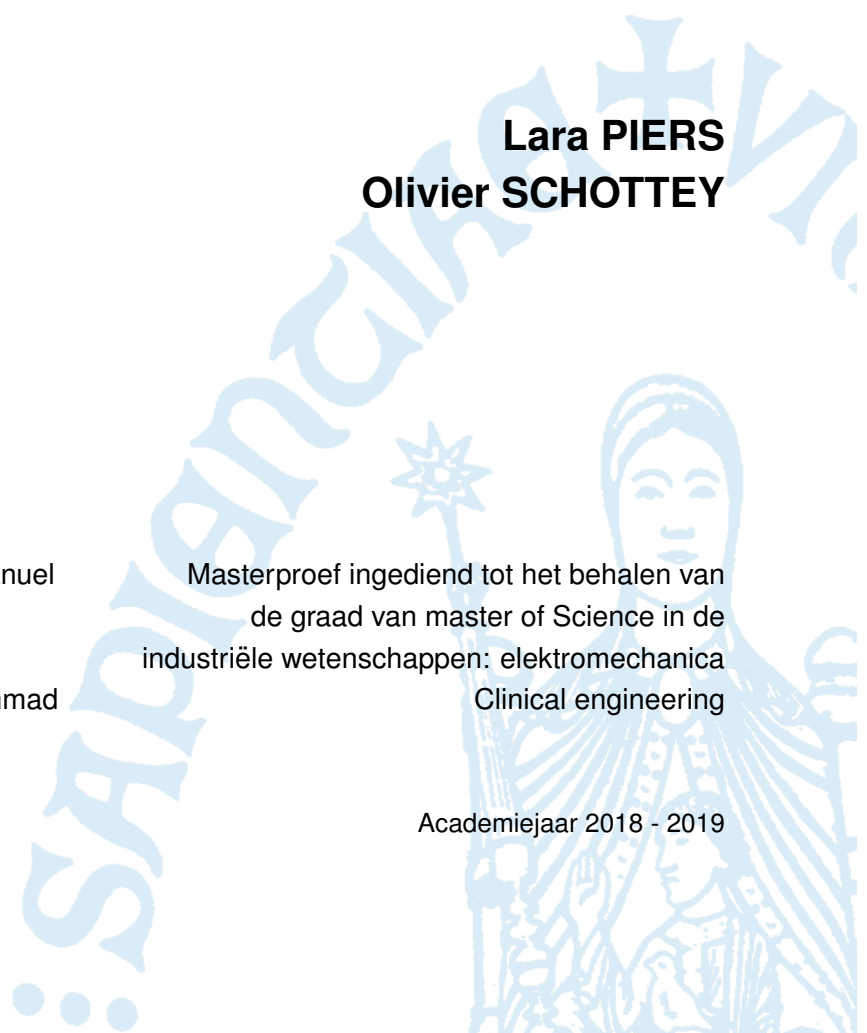
Lara PIERS
Olivier SCHOTTEY

Promotor: Prof. dr. ir. Emmanuel
Vander Poorten

Co-promotoren: ir. Mirza Awais Ahmad
dr. Luc Joyeux

Masterproef ingediend tot het behalen van
de graad van master of Science in de
industriële wetenschappen: elektromechanica
Clinical engineering

Academiejaar 2018 - 2019



©Copyright KU Leuven

Zonder voorafgaande schriftelijke toestemming van zowel de promotor(en) als de auteur(s) is overnemen, kopiëren, gebruiken of realiseren van deze uitgave of gedeelten ervan verboden. Voor aanvragen i.v.m. het overnemen en/of gebruik en/of realisatie van gedeelten uit deze publicatie, kan u zich richten tot KU Leuven Campus Groep T Leuven, Andreas Vesaliusstraat 13, B-3000 Leuven, +32 16 30 10 30 of via e-mail iiw.groept@kuleuven.be.

Voorafgaande schriftelijke toestemming van de promotor(en) is eveneens vereist voor het aanwenden van de in deze masterproef beschreven (originele) methoden, producten, schakelingen en programma's voor industrieel of commercieel nut en voor de inzending van deze publicatie ter deelname aan wetenschappelijke prijzen of wedstrijden.

Without written permission of the supervisor(s) and the author(s) it is forbidden to reproduce or adapt in any form or by any means any part of this publication. Requests for obtaining the right to reproduce or utilise parts of this publication should be addressed to KU Leuven, Technology Campus Groep T Leuven, Andreas Vesaliusstraat 13, B-3000 Leuven, +32 16 30 10 30 or via e-mail iiw.groept@kuleuven.be.

A written permission of the supervisor(s) is also required to use the methods, products, schematics and programs described in this work for industrial or commercial use, and for submitting this publication in scientific contests.

Acknowledgements

First of all, we would like to thank our co-supervisor ir. Mirza Awais Ahmad, PhD researcher at the biomechanics department of the KU Leuven, for the guidance he provided us throughout the year and for his trust and unrelenting motivation. Whenever we had a question or faced doubts, he was there to steer us in the right direction. Second, would like to thank our supervisor prof. dr. ir. Emmanuel Vander Poorten who took the time to give us extensive feedback on our work when we needed it and to provide coordination to bring our thesis project to a good end.

We are also deeply grateful to our second co-supervisor dr. Luc Joyeux, general pediatric surgeon and PhD researcher in fetal surgery at the urogenital, abdominal and plastic surgery unit of the KU Leuven for the time he gave us to give feedback on our work from a medical point of view. The medical knowledge dr. Joyeux passed on to us was of crucial importance for the success and medical relevance of our thesis.

In addition to our (co)-supervisor(s), we would also like to acknowledge the help we received from other PhD researchers of the biomechanics department of the KU Leuven. Particularly, we would like to thank Sergio Portolés Díez and Tom Vandebroek for their help regarding the functioning of the force sensor. Additionally, we would like to thank Qiao Qiao for her guidance in the creation of our spring model algorithm.

Throughout the year, we had the pleasure of working together with very motivated and kind colleagues who were also working to complete their thesis project. In particular, we would like to thank Nele Troonbeeckx for providing us with her force sensitive tool and to help us configure it. Additionally, we would like to thank Arthur Vanhulle, Jeroen Lambeau and Viktor Vörös for the times we spent in the lab together.

Finally, we would like to personally make some acknowledgements. Olivier would like to thank his family and friends for supporting and enduring him during the most testing times of this thesis. It was their patience and kindness that helped in delivering this thesis. In particular, he would like to dedicate this thesis to his late brother Mathieu Schottey, who motivated him in the past to face any challenge with unrelenting motivation.

Lara would like to thank her family who supported her during this thesis but mostly also throughout

her whole studies. She would also like to thank her friends who were there to help lift the pressure off her shoulders when it was most needed.

Samenvatting

Spina bifida (SB) of open rug is een aangeboren afwijking die in Europa bij gemiddeld 4,9 op 10 000 geboortes optreedt en wordt veroorzaakt door een niet-volledige sluiting van de neurale buis tijdens de embryonale ontwikkeling. Afhankelijk van de structuur, vorm en locatie van het defect kunnen de gevolgen variëren. Deze thesis focust zich op de meest ernstige en meest voorkomende vorm van SB namelijk spina bifida aperta, en meer specifiek de myelomeningocele (MMC), gekenmerkt door een vochtblaas op de rug waarin zich ruggenmerg en rugzenuwen bevinden.

Door langdurige blootstelling van deze laatsten aan de intra-uteriene omgeving of door schokken tijdens de zwangerschap of de bevalling, kan SB leiden tot onder meer motorische beperkingen of zelfs verlamming van de onderste ledematen. Het defect wordt meestal net na de geboorte gesloten. Om bovengenoemde schade aan ruggenmerg en zenuwen te beperken, kan het ook prenataal gesloten worden via een open buikoperatie. Deze ingreep heeft echter een hoog risico op ernstige complicaties voor zowel moeder als kind.

Een veelbelovend alternatief is de minimaal-invasieve, laparoscopische aanpak. Dit is een recente techniek die nog in volle ontwikkeling is. Gezien de complexiteit van deze ingreep en de ernstige gevolgen bij falen moet een chirurg een intensieve training ondergaan. Goede trainingsmodellen zijn schaars. Gedreven door het principe van de 3V's (vervanging, vermindering en verfijning) om zoveel mogelijk dierenproeven te vermijden, stelt deze thesis zich tot doel een synthetisch trainingsmodel met geïntegreerde sensoren te ontwikkelen. Op dit model kunnen chirurgen herhaaldelijk de minimaal-invasieve ingreep inoefenen. Na elk experiment kan beschadigd synthetisch materiaal vervangen worden. Dankzij geïntegreerde sensoren kunnen tijdens elke ingreep prestatieparameters opgemeten worden, welke gebruikt kunnen worden om de techniek te optimaliseren. Door over meerdere ingrepen deze parameters op te volgen kan een leercurve van een chirurg opgesteld worden.

In samenwerking met medische experts van het UZ Leuven werden de vereisten voor het model opgesteld. Deze volgden enerzijds uit de belangrijkste anatomische eigenschappen van het defect en de baarmoeder en anderzijds uit de specifieke uitdagingen gedurende de stappen van deze chirurgische interventie. Het model dient tevens de risico's van de operatie die samenhangen met blootstelling aan kwetsbare delen weer te geven. Het resulterende model bevat een synthetisch gedeelte met twee vervangbare stukken: de uteruswand en het defect. Het synthetisch MMC de-

fect laat de chirurg toe om de belangrijkste stappen van de operatie te oefenen. Verder bestaat het model uit een sensorisch gedeelte dat tijdens de training de belangrijkste parameters opmeet, namelijk: contact van instrumenten met het ruggenmerg en de rugzenuwen, de krachten uitgeoefend op de foetus en tot slot de verplaatsing van de instrumentpoorten in de uteruswand. Tijdens de interventie zal de chirurg met zijn instrumenten de uteruswand opspannen en vervormen wat mogelijk tot weefselschade en vroeggeboorte kan leiden. De eerste twee parameters worden rechtstreeks gemeten bij het defect door respectievelijk een eenvoudige elektrische schakeling en een krachtensor. De verplaatsing van de instrumentpoorten werd gemeten door de combinatie van bewegingssensoren en een algoritme.

Abstract

Spina bifida (SB) is a congenital malformation caused by embryonic failure in neurulation with a prevalence of 4,9 in 10 000 live births in Europe. Depending on the structure and location of the defect, the consequences of this malformation may vary. This thesis focuses on the most severe and most common form of SB which is spina bifida aperta (SBA), and more specifically myelomeningocele (MMC). This type of SB is characterized by a cyst containing the spinal cord and cerebrospinal fluid on the fetal back. Due to prolonged exposure of the spinal cord to the intra-uterine environment, SB can have lifelong consequences, including motor disfunctions going as far as paralysis of the lower limbs. The severity of the consequences can increase due to the impact of shocks during pregnancy and delivery on the spinal cord. In most cases, the defect is closed postnatally. To minimize the aforementioned damage to the spinal cord, the defect can alternatively be closed through open fetal surgery (OFS). This intervention, however, has a high risk of severe complications for both mother and child.

A promising alternative is the minimally invasive, fetoscopic approach. This is a recent technique which is still developing and which is only used in a few specialized centers across the world. Considering the complexity of this type of intervention and the severe consequences in case of failure, a surgeon must undergo intensive training. Good training models are scarce and, driven by the principle of the three *Rs* (replace, reduce, refine) to minimize the amount of animal trials in biomedical research, this thesis aims to develop a synthetic training model with embedded sensing. This training model can be used to practice the minimally invasive procedure repeatedly. After every training session, the synthetic material that was used can be easily replaced to prepare the model for a new intervention.

In cooperation with medical experts of the UZ Leuven, the requirements of the model were defined. The physical requirements of the model are, on the one hand, based on the most important anatomical properties of the MMC defect and the uterus, and on the other hand on the specific challenges encountered during the steps of the fetoscopic surgery. Additionally, the risks of the surgery leading to most severe consequences for mother and child were defined. Using the embedded sensing, this set of crucial performance parameters can be measured, which can be used to optimize the surgeon's technique. By collecting and reviewing this data over multiple surgeries, a learning curve of the surgeon can be established.

The resulting training model consists of a synthetic and a sensing portion. The synthetic portion features a detailed removable MMC defect, constructed out of several layers of silicone material, simulating the anatomy of its real-life counterpart. This defect is designed to simulate the dissection and closure steps of a fetoscopic repair of MMC. To compensate for the tensile stress the silicone undergoes during suturing, some of the layers are reinforced with medical compresses. Aside from the defect, the synthetic portion also features a simplistic uterine environment, incorporating a removable synthetic uterine wall.

The sensing portion features the measurement of three different parameters, namely the connectivity of the surgical instruments with the spinal cord, the forces exerted on the fetus and finally the displacement of the incision ports of the fetoscopic instruments. The development of a simple electronic circuit sensing the connectivity between the spinal cord and a fetoscopic instrument has been tested and validated to yield correct binary feedback. A force sensor was integrated into the synthetic section of the model. This integrated setup was subsequently tested and validated. It is able to compute forces exerted on the defect perpendicularly to it and can locate the origin point of these forces with an accuracy of 4 mm. During the fetoscopic intervention the surgeon will deform the uterine wall caused by the movements of these incision ports, which may lead to tissue damage and to iatrogenic preterm premature rupture of the membranes. Therefore, an algorithm was developed and tested that computes the displacement of the incision ports based on the position and orientation measurements of the fetoscopic instruments. Some further work was also done to create a numerical simulation of the synthetic uterine wall in the future. This simulation would estimate the forces exerted on and the subsequent deformation of the synthetic uterine wall caused by the displacement of the incision ports.

The result is thus a first version of a low-fidelity surgical training simulator which is able to simulate the main steps of the minimally invasive surgery and capable of measuring three critical parameters that could lead to severe consequences.

Keywords: Spina bifida, Myelomeningocele, Fetal therapy, Minimally invasive surgery, Surgical training simulator, Low-fidelity simulator

Contents

Acknowledgements	vi
Samenvatting	viii
Abstract	x
Contents	xii
List of figures	xv
List of tables	xvii
List of symbols	xix
List of abbreviations	xx
1 Introduction	1
2 Literature study	3
2.1 Defect	3
2.1.1 Embryology and anatomy	4
2.1.2 Treatment	6
3 Methodology	11
3.1 Synthetic model	11
3.1.1 Requirements for the synthetic removable defect	12
3.1.2 Requirements for the synthetic uterine environment	13
3.2 Sensing system	13
4 Development of a synthetic model and a sensing system	15
4.1 Development of a synthetic model	15
4.1.1 Removable defect	15

4.1.2	Uterine environment	20
4.1.3	Integration	22
4.2	Development of a sensing system	23
4.2.1	Connectivity	23
4.2.2	Forces on the uterine wall	25
4.2.3	Forces on fetus	45
5	Testing and validation	49
5.1	Validation of the synthetic model	49
5.1.1	Removable defect	50
5.1.2	Uterine environment	51
5.2	Validation of the sensing system	52
5.2.1	Connectivity	52
5.2.2	Forces on the uterine wall	53
5.2.3	Forces on the fetus	56
6	Future work	59
6.1	Synthetic model	59
6.2	Sensing system	60
7	Conclusion	61
7.1	Synthetic model	61
7.1.1	Removable defect	61
7.1.2	Uterine environment	62
7.2	Sensing system	63
7.2.1	Connectivity	63
7.2.2	Forces on uterine wall	63
7.2.3	Forces on fetus	63
A	Technical specifications of Ecoflex™	71
B	Specifications of Sylamed compresses	73
C	Technical specifications of Arduino Uno Rev3	75
D	Specifications and drawings of the 6-DOF force and torque sensor	77

List of Figures

2.1	Difference between spina bifida occulta, MMC and MC (source: The Sydney children's hospital network (http://www.schn.health.nsw.gov.au/))	3
2.2	Neurulation development and failure, creating a spina bifida defect (https://www.mayoclinic.org)	4
2.3	Cross-section of healthy spine (Marieb et al. (2015)).	5
2.4	Cross-section of a MMC defect (Bauman et al. (2016)).	5
2.5	Steps of open fetal surgery (Schematic drawings by Myrthe Boymans (www.myrtheboymans.nl)).	8
2.6	Separation of the skin from the fascia before suturing the skin (Sutton et al. (2015))	9
4.1	Illustration of the different mesh directions.	16
4.2	Example of silicone wire filled with stranded copper wires.	17
4.3	Cross-section of the removable defect.	17
4.4	Picture of the synthetic defect.	19
4.5	Exploded view of the synthetic defect.	19
4.6	An overview of the design of the uterine environment	20
4.7	The synthetic uterine wall is incorporated into the uterine environment by clamping it in between two square plates.	21
4.8	The pivoting arm has four attachment points, allowing for four different tilt configurations.	22
4.9	The synthetic uterine wall is incorporated into the uterine environment by clamping it in between two square plates.	23
4.10	Electrical network of setup made to sense contact with spinal nerves	25
4.11	Picture of the position tracking setup	26
4.12	The calibration procedure of a surgical instrument is completed by attaching an Aurora sensor to the instrument's handle and by holding a second Aurora sensor at its tip.	27

4.13	The synthetic uterine wall clamp contains three premade holes which are used for landmarking the incision plane. To complete the landmarking procedure, these three holes must be touched with the tip of a calibrated instrument. Touching point A stores the location of \mathbf{p}_{planeA} , touching points B and C stores those of \mathbf{p}_{planeB} and \mathbf{p}_{planeC} , respectively.	28
4.14	Graphical interpretation of the calculations leading up to (4.10). In the case shown on the figure, \mathbf{v} is perpendicular to the normal vector of the plane \mathbf{n}	29
4.15	The synthetic uterine wall we want to simulate has a circular shape and is clamped along the outer edge.	32
4.16	Mesh results for a circular geometry (radius = 90 mm) using the distgrid function with a progressively lower value for h_0 : (a) 75 nodes ($h_0 = 20$ mm), (b) 131 nodes ($h_0 = 15$ mm), (c) 295 nodes ($h_0 = 10$ mm), (d) 1177 nodes ($h_0 = 5$ mm)	33
4.17	Mesh results using two preallocated points, with 133 nodes ($h_0 = 15$ mm): two pre-allocated points annotated in blue, their neighbouring nodes annotated in red and the boundary nodes annotated in green.	34
4.18	A static equilibrium of a spring model ($h_0 = 15$ mm, $N = 133$, $k = 60$ N/m) with two preallocated nodes found after applying a force of -1 N along the x-axis to the left preallocated node and a force of 1 N along the axis to the right preallocated node.	35
4.19	A test spring model with a preallocated node at the center.	37
4.20	The influence of the h_0 and k parameters on the displacement of a node in the spring network after being affected by a force of 1 N.	38
4.21	A photo of the instrument developed by Nele Troonbeeckx.	38
4.22	An illustration of the instrument developed by Nele Troonbeeckx.	39
4.23	The loading case of figure 4.22 split up into a case of pure force and pure moment loading.	39
4.24	The set-up of the pure force experiment to calibrate the force sensing instrument.	40
4.25	The results of exerting pure force on the force sensing instrument	41
4.26	An illustration of the pure moment experiment to calibrate the force sensing instrument.	41
4.27	The results of exerting pure moment on the force sensing instrument	42
4.28	The set-up of the spring model calibration experiment.	42
4.29	The trajectory and absolute displacement of the incision point caused by the operator moving to the left.	43
4.30	Strain measurements taken with the force sensitive instrument for a portion of the trajectory shown in figure 4.29 and the corresponding computed forces and moments.	44
4.31	Computed measurements from the calibration experiment with the force sensitive instrument	45
4.32	Set-up for the recording of data from the force and torque sensor.	46

4.33	Illustration of forces and torques directions.	46
4.34	Orientation of defect with respect to coordinates of the sensor.	46
4.35	Behaviour of F_z , T_y and T_x with increasing load.	47
5.1	A photo taking during the test surgery.	49
5.2	Sight of the defect after cutting out the placode.	50
5.3	Sight of the defect after removal of the zona epitheliosa during the test surgery.	50
5.4	Sight of the defect during undermining.	51
5.5	Sight of the defect after removal of the zona epitheliosa during the test surgery.	51
5.6	Electrical network of the test setup.	52
5.7	A side-by-side comparison showcasing the algorithm which is able to turn position and orientation measurements of an instrument's handle into motion of the entire instrument.	54
5.8	A sequence of plots showing the incision port motion due to translational motion of a surgical instrument. The surgical instrument is shown in the figure as the thick black line.	55
5.9	Location of the forces during the cutting steps.	57
5.10	Location of the forces during suturing	57

List of Tables

1.1	The three <i>Rs</i> of biomedical research involving work with animals	2
3.1	Summary of the main steps of the fetoscopic surgery.	11
3.2	List of requirements for the removable defect site.	12
4.1	Steps to make the different layers of the defect.	18
4.2	Price of the removable defect.	19
7.1	List of requirements for the removable defect site. This is a copy of table 3.2.	61

List of symbols

d	Distance	$[m]$
d_{ab}	Distance between node a and b	$[mm]$
d_x	x coordinate of the location where the force is applied	$[m]$
d_y	y coordinate of the location where the force is applied	$[m]$
g	Gravitational constant	$[m/s^2]$
h_0	Initial distance between nodes	$[mm]$
k	Spring constant	$[N/m]$
m	Mass	$[kg]$
n	Normal vector of the incision plane	$[-]$
p_a	Position vector of point a	$[-]$
p_b	Position vector of point b	$[-]$
p_{handle}	Position vector of the handle of the instrument	$[-]$
p_{inst}	Position array of instrument handle and tip measurements	$[-]$
p_{line}	Position vector of any point along the line containing u	$[-]$
p_{planeA}	Position vector of landmarking point A	$[-]$
p_{planeB}	Position vector of landmarking point B	$[-]$
p_{planeC}	Position vector of landmarking point C	$[-]$
p_{planeO}	Position vector of the origin of 2D reference coordinate system	$[-]$
p_{port}	Position vector of incision port	$[-]$
p_{sensor}	Position vector of the Aurora sensor	$[-]$
p_{tip}	Position vector of the tip of the instrument	$[-]$
q	The quaternion expressing the orientation of the Aurora sensor	$[-]$
s	Scalar representing the fraction of p_{line} 's position along u	$[-]$
u	Vector representing the line segment between handle and tip	$[-]$
v	The vector from p_{planeA} to a variable point on the line containing u	$[-]$
v_1	Linearly independent vector in the incision plane	$[-]$
v_2	Linearly independent vector in the incision plane	$[-]$
w	Vector representing the line segment between handle and p_{planeA}	$[-]$
C_1	Calibration constant 1	Nm/μ_{strain}
C_2	Calibration constant 2	Nm/μ_{strain}
C_3	Calibration constant 3	Nm/μ_{strain}

C_4	Calibration constant 4	$\text{Nm}/\mu\text{strain}$
F	Force	$[N]$
F_a	Total force acting on p_a	$[N]$
F_{ab}	Spring force acting on p_a	$[N]$
F_{ext}	External force(s)	$[N]$
F_{moment}	Internal force contribution due to bending moment	$[N]$
F_r	Resulting lateral force caused by a moment on an off-center pivot point	$[N]$
F_x	Force along the x-axis of the sensor	$[N]$
F_y	Force along the y-axis of the sensor	$[N]$
F_z	Force along the z-axis of the sensor	$[N]$
I	Identity matrix	$[A]$
I_{pin}	Current at the pin of the arduino	$[A]$
L	Length	$[m]$
L_0	Distance between force and half bridge A_0	$[cm]$
L_0	Resting length of spring A_0	$[mm]$
L_1	Distance between force and half bridge A_1	$[cm]$
M_F	Moment caused by premeasured weights	$[Nm]$
$M_{measured}$	Bending moment measured by force sensing instrument	$[Nm]$
M_{0F}	Bending moment experienced by strain gauge A_0	$[Nm]$
M_{1F}	Bending moment experienced by strain gauge A_1	$[Nm]$
N	Amount of nodes in spring network	$[-]$
R	Radius of circle	$[mm]$
R_1	Resistance of resistor 1	$[\Omega]$
R_3	Resistance of resistor 3	$[\Omega]$
S_{plane1}	A set of linearly independent vectors in the incision plane	$[-]$
S_{plane2}	An orthogonal basis of the incision plane	$[-]$
T_x	Torque around the x-axis of the sensor	$[Nm]$
T_y	Torque around the y-axis of the sensor	$[Nm]$
T_z	Torque around the z-axis of the sensor	$[Nm]$
${}^{World}T_{Handle}$	Transformation matrix from world to the handle of the surgical instrument	$[-]$
${}^{World}T_{Tip}$	Transformation matrix from world to the tip of the surgical instrument	$[-]$
V_{in}	Voltage at the pin of the arduino	$[V]$
ϵ_{pos}	Error vector of the displacement of preallocated nodes in the spring network	$[-]$
ϵ_0	Strain measured by half bridge A_0	$[-]$
ϵ_1	Strain measured by half bridge A_1	$[-]$
ϵ_{0F}	Strain measured by half bridge A_0 due to pure force	$[-]$
ϵ_{1F}	Strain measured by half bridge A_1 due to pure force	$[-]$
ϵ_{0M}	Strain measured by half bridge A_0 due to pure moment	$[-]$
ϵ_{1M}	Strain measured by half bridge A_1 due to pure moment	$[-]$

List of Abbreviations

AWG	American Wire Gauge
CNS	Central Nervous System
CSF	Cerebrospinal Fluid
DOF	Degree Of Freedom
EtherCAT	Ethernet for Control Automation Technology
FPGA	Field-Programmable Gate Array
iPPROM	iatrogenic Preterm Prelabor Rupture Of Membranes
MC	Meningocele
MIS	Minimally Invasive Surgery
MMC	Myelomeningocele
MOMS	Management of Myelomeningocele Study
MSM	Mass Spring Model
NDI	Northern Digital Inc.
NI	National Instruments
NTD	Neural Tube defect
OFS	Open Fetal Surgery
PFG	Planar Field Generator
ROS	Robot Operating System
SB	Spina Bifida
SBA	Spina Bifida Aperta
SBO	Spina Bifida Occulta

SCU	System Control Unit
TTTS	Twin-to-Twin Transfusion Syndrome

Chapter 1

Introduction

Spina bifida (SB) is a congenital malformation caused by the failure of a complete closure of the neural tube during neurulation. This can lead to lifelong consequences for those affected, both physically and cognitively. The specific consequences vary based on the structure and location of the defect. Spina bifida aperta (SBA), the most common and severe form of SB, is addressed in this thesis. The current methods to treat SB are to either close the defect postnatally, or prenatally by open fetal surgery. Both methods, however, have major disadvantages. By reducing invasiveness, the influence of these disadvantages would most likely be decreased. Therefore, a minimally invasive approach is being considered. This type of surgery, however is very complex due to the restrained motion of the surgeon and requires a lot of training.

Currently, this training is done by first training on low-fidelity simulators, initially to learn basic manipulations with minimally invasive instruments and later on to train more complex tasks. The next step in the training is to move on to higher fidelity models, usually in the form of animal models. One of the animal models that is being used to train the minimally invasive SBA intervention that we have encountered while working on this project, is a rabbit model. This model is used because the abdominal cavity of a rabbit is approximately the same size of a human uterus at about 20 weeks of gestation, approximately the median gestational age at which the fetoscopic intervention would take place. When practicing on this model, the stomach of rabbit serves as the simulation for the fetal back, onto which a patch is sutured and subsequently tested for watertightness. A second, higher fidelity model that is being used to train the same intervention is that of a pregnant sheep. In this model, the sheep fetus is approximately the same size of a human fetus at 20 weeks of gestation. When practicing on this model, a piece of marked skin on the back of the fetus would serve as the simulation for a SB defect.

It is an obvious necessity to train on these high-fidelity models before being able to move on to human cases. However, driven by the three *Rs* of medical research involving work with animals (table 1.1), we introduce our thesis project. The goal of our thesis is to create a low fidelity synthetic model that simulates the most complex steps of a fetoscopic SB intervention. To make this synthetic model as cost-effective as possible, we aim to make some parts of this synthetic model replaceable instead of using a different model for every surgery. As an added value, we aim to introduce an

evaluation method in the model. This evaluation method would rely on a set of objective parameters that would be measured by embedded sensing in the model. This could make it possible to score the performance of a surgeon and to see their learning curve over multiple surgeries.

Replace	Work without animals whenever possible.
Reduce	When you cannot avoid the use of animals, use as few as possible.
Refine	Optimize the process to minimize harm done to the animal.

Table 1.1 The three *Rs* of biomedical research involving work with animals

While our low-fidelity simulator will not directly replace any of the high-fidelity models, our hope is that down the line, the necessity of the number of animals used in the training process might be reduced by the creation of a simulator that specifically trains for the steps of the surgery.

Chapter 2

Literature study

2.1 Defect

Neural tube defects (NTD's) are anomalies occurring during the development or closure of the neural tube. They are the most common severe congenital malformations of the nervous system with a prevalence of 4,9 in 10 000 live births in Europe (Joyeux et al. (2018)). The prevalence is strongly dependent on geographic location and can be as high as 1 % in less developed areas. Spina bifida (SB) is one of the most frequent types of NTD's (together with anencephaly). It is a failure in the closure of the neural tube on the caudal side. Depending on the severity and structure, it can be further sub-categorized into aperta and occulta. Spina bifida aperta (SBA) is the malformation focused on in this study and means that the defect is open which, in contrast with spina bifida occulta (SBO), is a life threatening condition. It almost always comes together with physical and cognitive functions disabilities. The most common consequences are motor restraints of the lower limbs going as far as paralysis, bowel and bladder dysfunction, hydrocephalus and a tethered spinal cord. SBA can have many different shapes with most frequent being myelomeningocele (MMC) followed by meningocele (MC). MMC is a herniation of neural tissue through the skin and defective bone. MC is a protrusion of the meninges through the defect, but it has no neural involvement (Sutton et al. (2015); Song et al. (2016)). Figure 2.1 shows the difference between SBO and the two most frequent types of SBA, the MMC and the MC.

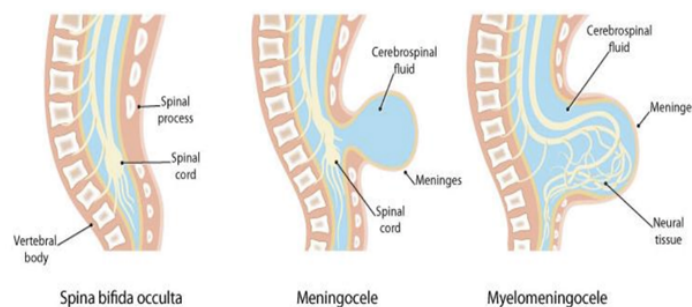


Figure 2.1: Difference between spina bifida occulta, MMC and MC (source: The Sydney children's hospital network (<http://www.schn.health.nsw.gov.au/>))

In further explanations, the terms neural tube defect and spinal dysraphism will be used as synonyms of spina bifida aperta.

2.1.1 Embryology and anatomy

One of the first stages in the development of a fetus is neurulation. Neurulation is a process happening at three weeks of development which forms the neural tube. This neural tube will later develop to become the spinal cord and the brain. Before neurulation, the fetus is shaped as an oval plate called the neural plate. During neurulation, this neural plate folds and fuses along the mid-line to create a hollow tube called the neural tube. This fusion then extends like a zipper caudally and cranially simultaneously as shown on figure 2.2.

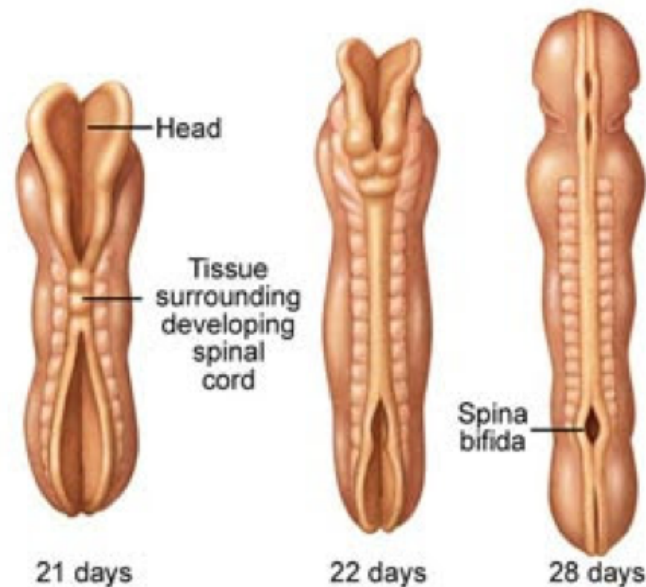


Figure 2.2: Neurulation development and failure, creating a spina bifida defect (<https://www.mayoclinic.org>)

In the case of SBA, the fusion fails in the lumbar area in most cases, leading to a deficiency in the skin, fascia, muscle and bone at that place. It is important to understand the different layers that are deficient to later understand the surgery. In the normal case, the spinal cord is protected by meninges, bone of the vertebra, muscles, fascia, fat and skin (Dickson et al. (2009)). Figure 2.3 shows a cross-section of a healthy spine. This figure only shows the bones and spinal cord. The posterior part of the vertebra is covered with muscles and then skin.

The meninges are three membranes surrounding the spinal cord. The external membrane of the meninges is called the dura. The fascia is connective tissue that attaches muscles, bone and skin to each other. To be able to compare the anomaly with a healthy spine, a cross section of the anatomy of an MMC is shown on figure 2.4. First, one can see that the posterior part of the vertebra is missing. Depending on the severity and location of the NTD, one or several posterior vertebrae can be deformed. Secondly, one can observe that instead of being a cylindrically shaped membrane contained between bones, the dura is not completely closed and is herniated to the

surface. The third major difference with a normal spine is the open skin and fascia, which leads to the exposure of neural matter. Finally, on figure 2.4, we see that the MMC is characterized by a cyst filled with cerebrospinal fluid (CSF) with on top of it the placode. The placode is a piece of embryonic neural plate that did not neurulate (Gupta et al. (2013)). The remaining exposed membranous surface around the placode is called the zona epitheliosa.

To sum up, the major differences between a MMC and a normal spine, which are responsible for the severe consequences of SB, are the opening in the skin, fascia and dura. These layers are essential for the proper protection of neural matter from the intra-uterine environment and shocks during labor and post-natal life (Adzick et al. (2011)).

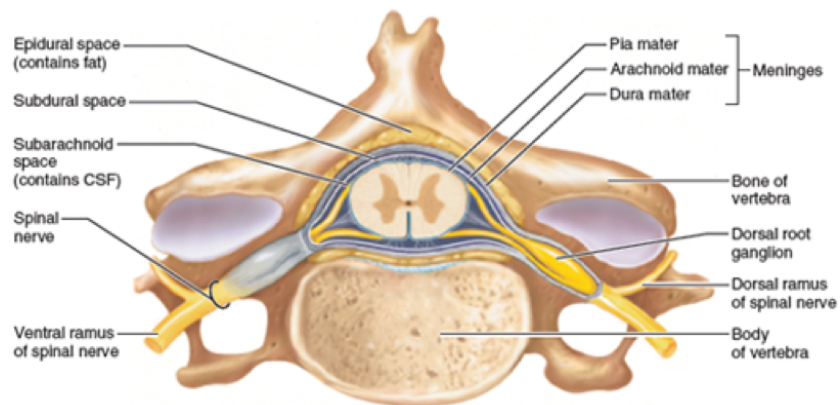


Figure 2.3: Cross-section of healthy spine (Marieb et al. (2015)).

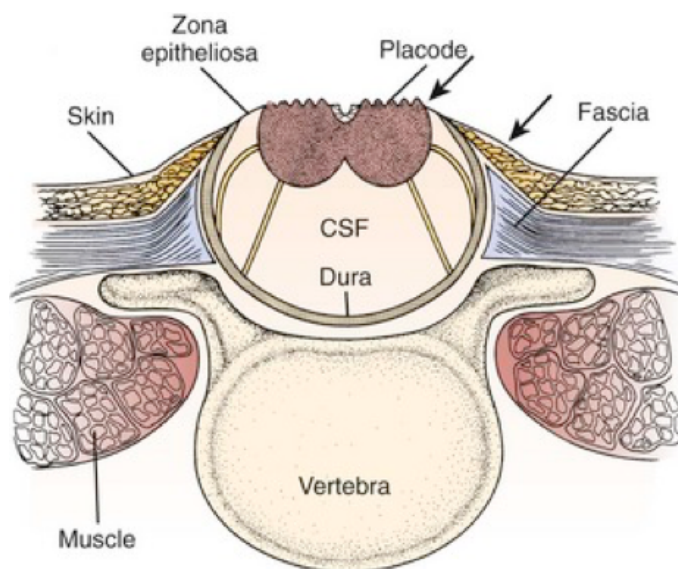


Figure 2.4: Cross-section of a MMC defect (Bauman et al. (2016)).

As mentioned before, the main consequences of SBA are related to motor and cognitive functions. These are consequences of damage to the central nervous system (CNS) and of a deformity of the

spine (Foster and Goldstein (2017)). More specifically, SBA almost inevitably comes together with Chiari II and hydrocephalus malformations. Chiari II is a hindbrain herniation that leads to symptoms like balance and coordination difficulties, apnea and swallowing difficulties (Gupta and Ross (2017); Cai and Jerry Oakes (2006)). The hindbrain herniation is caused by a pressure difference in the CSF between the brain and the spinal cord. The cause of this pressure difference is the leakage of CSF through the placode (Cai and Jerry Oakes (2006)). The Chiari II malformation also forms an obstruction to the CSF flow which leads to hydrocephalus, a condition characterized by an accumulation of CSF in the brain that causes intra-cranial compression (Williams (2008)). It affects 70 % to 85 % of the patients with MMC (Gupta and Ross (2017)).

Finally, additional disabilities follow from the progressive degeneration of nervous tissues due to prolonged exposure to the intra-uterine environment. Shocks received during pregnancy and delivery can permanently damage the spinal cord as well. These additional conditions are, for example, restricted motor functions or paralysis and deformity of the lower limbs. Also, bowel and bladder malfunctions and sensory loss are often consequences of the degeneration of nervous tissues. NTD's are also frequently associated with a tethered spinal cord syndrome. This syndrome forces the spinal cord to stretch during growth and movements because it can not move freely. The consequences of this syndrome get worse as the child ages.

2.1.2 Treatment

Proper treatment and adapted therapy are crucial for the survival of the patients. In most developed countries, methodical screening and improving imaging technologies allow an early diagnosis of SBA (Joyeux et al. (2018)). The predominant diagnostic techniques used are fetal MRI and ultrasonography because of the detailed image they create. The MRI shows the anatomy of the CNS and the presence of hindbrain herniation. Whereas the ultrasound is used to observe other anomalies, leg movement and the structure of the MMC (Heuer et al. (2014)). Following from the diagnosis, a lot of pregnancies proceed to an elective termination, which explains the low prevalence in Europe compared to countries where detection is less regulated.

When treating a newborn with SBA, the first step is to close the defect as soon as possible to protect the CNS from the environment. During this surgery, the spinal cord is also untethered. In most cases, this happens within 48 hours after birth. The disadvantage of this method is that the damage done to the spinal cord during gestation and labor is irreversible. To counter this, another possibility is to close the defect prenatally by means of an open surgery at around 20 weeks of gestation. But still, open surgery comes with an increased risk of preterm delivery and uterine dehiscence (Adzick et al. (2011)). To reduce invasiveness, a new approach is being considered, the fetoscopic surgery. More detailed explanation about the open surgery and fetoscopic surgery and their consequences can be found in sections 2.1.2.1 and 2.1.2.2.

Secondly, the additional disabilities need to be treated as well. Hydrocephalus often requires a neurosurgical intervention for the placement of a shunt to restore normal CSF circulation. Lower

limb malformations require surgery and intensive physical therapy (Gupta and Ross (2017); Foster and Goldstein (2017)). Even if the spinal cord is untethered during surgery, often the scar tissues get retethered afterward during the healing process. The consequence of this is the degeneration of some abilities controlled by the CNS as the patient gets older. In that case, an additional surgery is required (Wang and Bierbrauer (2017)).

2.1.2.1 Open fetal surgery

Open fetal surgery (OFS) has been considered as a way to treat SBA prenatally because of the degenerative damage caused to the spinal nerves during pregnancy that can lead to the aggravation of hindbrain herniation and hydrocephalus and to loss of lower limb movement. The first reported open surgery on an MMC defect was performed in the late 90's. The success of this surgery led to the continued usage of this method in carefully selected cases. Early data collected from these surgeries was promising and led to the start of a randomized study, the Management of Myelomeningocele Study (MOMS) (Adzick et al. (2011)). The aim was to compare prenatal and postnatal closure of MMC. The study was conducted in three specialized centers, the Children's Hospital of Philadelphia, Vanderbilt University, and the University of California, San Francisco. It was conducted on 158 patients chosen randomly, of which 50 % underwent a fetal open surgery and the remaining 50 % postnatal surgery. All prenatal surgeries happened before 26 weeks of gestation. The two main evaluation criteria for the outcome were the need for CSF shunting at 12 months of age and mental development and motor functions at 30 months.

The conclusions of the MOMS trial show that a prenatal surgery to treat MMC improves motor function and mental development at 30 months and also reduces the need for shunting at 12 months. Additionally, prenatal closure seemed to result in less severe Chiari II malformations and an increased likelihood of the patient being able to walk independently later on in life. However, the study also concludes that prenatal surgery is associated with increased maternal and fetal risks. The most common consequences are a uterine dehiscence and preterm birth due to the damage caused to the uterine wall (Adzick et al. (2011)).

Figure 2.5 shows the steps followed during open fetal surgery. When referring to figures A to H in this paragraph, we mean the sub-figures of Figure 2.5. The first step is to position the fetus so that the defect is located at the opening of the hysterotomy as seen on figure B. Then the placode is carefully untethered by cutting the tissue around it (dashed green line on figure A) which will make the placode drop back into the spinal canal. This first cut will also let the surplus fluid inside the cyst escape. The excess zona epitheliosa is then cut away at the junction between the skin and the zona epitheliosa (blue dashed line on figure A). These two steps can be seen on figure E. Figure C represents the initial MMC defect, whereas figure D represents another kind of SB, which is irrelevant for this study. Next, each layer has to be closed separately like on figure F, first the placode, then the fascia and finally the skin. To close the skin, the skin has first to be separated from the fascia by undermining it radially for 2 cm, as can be seen on figure 2.6 (Joyeux et al. (2018); Sutton et al. (2015)).

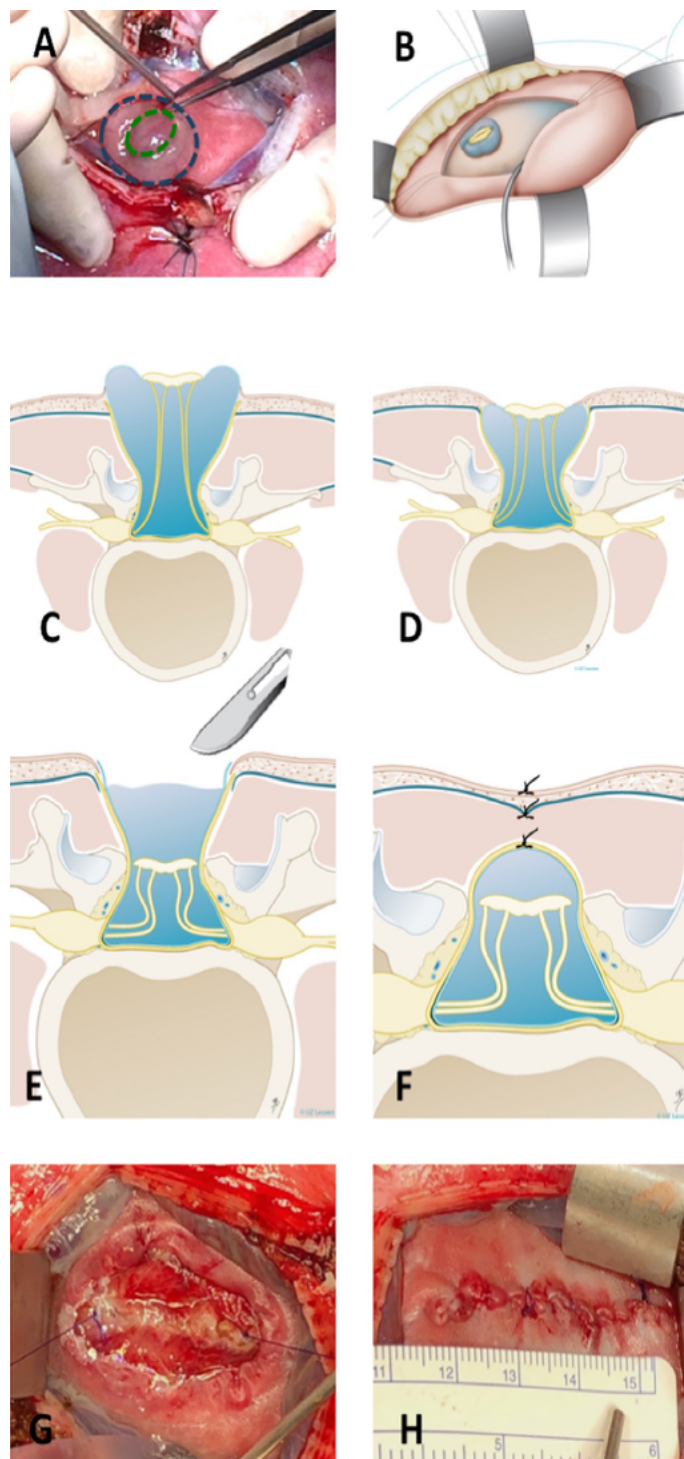


Figure 2.5: Steps of open fetal surgery (Schematic drawings by Myrthe Boymans (www.myrtheboymans.nl)).

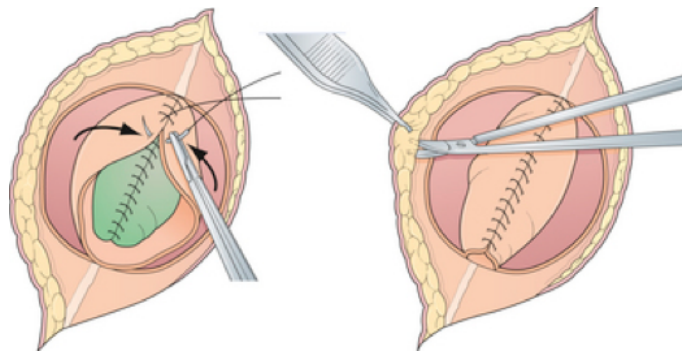


Figure 2.6: Separation of the skin from the fascia before suturing the skin (Sutton et al. (2015))

2.1.2.2 Fetoscopic surgery

Fetoscopy is a kind of minimally invasive surgery (MIS) or keyhole surgery that is specific to the surgery on a fetus. It is characterized by the insertion of surgical instruments through one, two or three ports that have a diameter of about 1,5 cm.

In 1994, before the first OFS, the first attempts to close an MMC by fetoscopy in humans were performed. The results were, however, not promising, with an increased mortality rate and need for shunting (Sutton et al. (2015)). The steps of the fetal surgery are exactly the same as for the postnatal surgery but prenatal interventions require more preparation to access the defect site on the back of the fetus. The first additional step is the exteriorization of the uterus and the positioning of the fetus. Secondly the incisions are made in the uterus and the cannula(e) is inserted. Finally, the uterus is insufflated.

Despite the initial setbacks, the minimally invasive approach has been tried again in the past few years and the outcome of more than 200 fetoscopic surgeries have been reported. Conclusions can only be taken when all the surgeries are executed in the same way, which is not the case. Despite that, it is a fact that fetoscopy is a challenging and long lasting intervention that requires a lot of training to acquire the necessary skills (Joyeux et al. (2018)). Stages of training involve first learning basic manipulation and coordination skills, followed by the training of specific tasks for a minimally invasive intervention. This training is sometimes performed on models of organic composition, either ex-vivo or in-vivo. In-vivo models involve animal models, like the one validated in (Peiro et al. (2013)) to train for fetoscopic MMC repair. However, these animal models often come with both logistical issues and ethical concerns, the last regarding the three *Rs* of biomedical research (Goldberg et al. (1996)). An alternative to organic models is the use of nonorganic surgical trainers. Nonorganic models are classified as low-fidelity simulators, whereas organic models are classified as high-fidelity simulators. These low-fidelity simulators partially recreate operative conditions and allow the surgeon to make progress along the learning curve before they move on to higher fidelity organic models (Munz et al. (2004)).

Types of nonorganic models include box trainers, mixed-reality trainers and synthetic models. Box trainers allow a trainee to learn the psychomotor skills, such as basic manipulation skills with laparoscopic instruments, judgement of depth perception based on two dimensional visuals, handling of a video endoscope and hand-eye coordination based on video feedback (Derossis et al. (1998); Aggarwal et al. (2004)). A mixed-reality surgical trainer combines virtual reality with the benefits of a box trainer. An example of this is the mixed-reality surgical trainer for fetal laser minimally invasive surgery, to treat twin-to-twin transfusion syndrome (TTTS) developed in (Javaux et al. (2018)). The model they developed trains surgeons for both basic fetoscopic skills and tasks specific to the TTTS intervention. Synthetic models offer surgeons a reproducible way to train certain skills or surgery steps. Two examples of such synthetic models to train for fetoscopic repair of MMC are those developed in (Miller et al. (2018)) and (Belfort et al. (2018)). While these allow to train for some steps of the surgery, they do not incorporate a MMC defect with detailed anatomical features.

Chapter 3

Methodology

We were guided in the creation of our training model by medical experts, predominantly dr. Luc Joyeux, from the UZ Leuven. This interdisciplinary collaboration was essential to gather an objective list of requirements for the model to maximize its quality as a surgical simulator and its potential contribution to the medical field. Additionally, their feedback was indispensable to decide which parameters our integrated sensing system would measure.

3.1 Synthetic model

The most important guideline we used for creating our synthetic model and its features were the steps of the fetoscopic surgery it is trying to simulate. A summarized version of these steps is given in table 3.1.

Step 1	Uterine exteriorization and fetal positioning.
Step 2	Uterine incision and incertion of cannula(e).
Step 3	Uterine insufflation.
Step 4	Untethering of the placode from the zona epitheliosa.
Step 5	Incision at the junction between skin and zona epitheliosa to remove excess zona epitheliosa.
Step 6	Closure of the dura and fascia.
Step 7	Undermining the skin from fascia at 2 cm around the defect.
Step 8	Closure and suturing of the skin.

Table 3.1 Summary of the main steps of the fetoscopic surgery.

The back-and-forth between our teams yielded a good indication of what the most important characteristics were that should be included in our synthetic uterus model, and which could be left out. What became clear is that the most important steps of the training procedure are the ones performed at the level of the SBA defect (steps 4 through 8). Our medical experts agreed that this contained the core of the surgery training and that it is the quality of the defect and the ability to perform the different steps on it that would dictate the quality of the model as a trainer. This

allowed us to split up the synthetic model into a detailed synthetic defect and a more rudimentary synthetic uterine environment. The fact that we could reduce the rest of the uterine environment to its essence, allowed the cost to be minimized and the functionality to be maximized.

The synthetic part of the training model should simulate the selected steps of the surgery as qualitatively as possible. Over several iterations of the synthetic model, we validated this quality by showcasing our progress to our medical experts and adjusting our designs according to their feedback.

3.1.1 Requirements for the synthetic removable defect

The requirements for the removable defect follow from the steps of the surgery and from the chosen measurement parameters and are listed in table 3.2. The driving force behind every choice is to make the defect as cheap as possible. As shown, the defect should most importantly feature a layered design and the ability to withstand suturing manipulations without tearing. There should be several layers that can resist suturing since at least two membranes need to be closed during the surgery. Realistic dimensions of the malformation resulted from a meeting with the medical experts of the UZ Leuven. Moreover, the size of the whole synthetic defect should be big enough to detach the skin from the fascia all around the defect, up to 2 cm away from the junction between the skin and the zona epitheliosa. Since we want to sense the contact of the surgical instruments, the nerves need to be modelled. The presence of a cyst is necessary to mimic a MMC defect which is more complicated to repair, than for example a MC defect, due to the herniation of the placode and nerves into the cyst. We believe that it is more interesting to practice on a more difficult type of SB. The next requirement is the presence of a distinguishable placode to make the synthetic defect resemble the real one. Finally, being able to fill the cyst with liquid, makes the model more realistic.

Requirements	priority
As cheap as possible	High
Multiple layers	High
Suturable without tearing	High
Defect size: 4 x 2 cm	High
Separable layers at a radius of 2 cm around the defect	High
Modelled nerves	High
Presence of a cyst	Medium
Distinguishable placode	Medium
Cyst filled with liquid	Low

Table 3.2 List of requirements for the removable defect site.

3.1.2 Requirements for the synthetic uterine environment

As mentioned before, we agreed with our medical experts to simplify the uterine environment. For example, we decided to leave out the steps concerning the exposure and insufflation of the uterus and the positioning of the fetus. While these steps have to be performed in the actual surgery, they are not unique to the intervention. We chose to leave them out because this lowers the cost of the training model, while still focusing on the most important part (closure of the defect) of the surgery. However, apart from the simplifications, it became apparent that three characteristics that involve or are related to the uterine environment could become important features of the training model.

- The distance to the defect on the fetal back from the uterine wall (the location where the surgeon's instrument incision points are located) should be between 10 and 15 cm, according to the surgeon.
- At this point it is uncertain which is the superior technique to use in the minimally invasive surgery; a single port, double port or triple port approach. We want to provide flexibility to account for this uncertainty by giving the surgeons the option to train whichever approach they prefer.
- The working area for the surgeon on the outside of the uterus, in which his instrument ports and instrument handles are located during the surgery, corresponds to a circular zone with a diameter of approximately 18 centimeters. The uterus model should offer the surgeon a similar working area.

3.2 Sensing system

In most surgeries, some objective (time, usage of anesthetic/CO₂) and subjective (performance) parameters can be used to score the surgical team. To build on this, we wanted to incorporate a sensing system in our synthetic model that measures additional objective data during a training session. Combining what we know from the anatomy of the defect and fetus and from our collaboration with the medical experts, we compiled a list of three objective parameters we wanted to measure with our sensing system.

- First, we wanted to capture any contact of the surgeon's instruments with the spinal cord and placode of the fetal MMC defect, as this, according to our experts, may cause irreparable damage to the unborn child.
- Second, we wanted to measure the impact on the uterine wall caused by the manipulations the surgeon performs with his fetoscopic instruments. In some cases, this may lead to iatrogenic preterm prelabor rupture of membranes (iPPROM) (Beck et al. (2012)).
- As a third parameter, we wanted to measure the forces the surgeon exerts on the defect. Because the defect is located on the back of the fetus in real life, this gives a measure of which forces are exerted on the fetus.

Throughout our development, we selected the technologies for the sensing part of the training model by availability, data output and the ability to expand on in the future. We validated their functioning by experiments.

Chapter 4

Development of a synthetic model and a sensing system

4.1 Development of a synthetic model

We designed a low fidelity training model or 'phantom' which can be used to practice the most complex steps of the fetoscopic intervention for prenatal SBA (MMC) closure. For this purpose, it features a detailed synthetic defect, designed specifically to simulate the steps that occur in the closure of an in-vivo MMC defect. In addition to the defect, the training model features a simplistic environment with a removable synthetic uterine wall that can be pivoted into different positions around the defect. The focus of this uterine environment is functionality and cost minimization.

4.1.1 Removable defect

The synthetic defect was designed based on the anatomy of the malformation and on the steps of the surgery. Surgeons should be able to practice the main steps of the surgery on the model. The list of requirements that led to this design can be found in chapter 3. To get to the final design, several iterations were needed based on the feedback of medical experts of the UZ Leuven on the different prototypes. The defect has a circular shape with a diameter of 15 cm. Each layer is made out of Ecoflex™ 00-50 which is a kind of silicone. The technical specifications of this silicone can be found in appendix A. The amount needed for each layer is calculated from the density of Ecoflex™ and the thickness wanted for that layer. The specific volume is given by the specifications of appendix A and is equal to 25,9 cu.in./lb., which corresponds to 1068,7 kg/m³.

Only the layers that need to be sutured (dura and skin) are reinforced with mesh to prevent the Ecoflex™ from tearing during suturing. For this mesh, we use non-sterile non-woven medical compresses from the company Sylamed. More specifically, the model of this compresses is Sylasoft with dimensions of 7,5 x 7,5 cm which are four folded (reference: 113). More information can be found in appendix B. The dimensions of 7,5 x 7,5 cm given by the specifications are the dimensions of the compress when it is folded. In its unfolded form it is a square with sides of 15 cm, which

is the limiting dimension for the whole defect. Attention must be paid to the direction in which the mesh is placed. The stiffness is much higher in one direction than the other. As there should be enough elasticity in the horizontal direction to close the defect, the mesh is oriented so that stiffer direction is the vertical one. Figure 4.1 shows the orientation of the mesh.

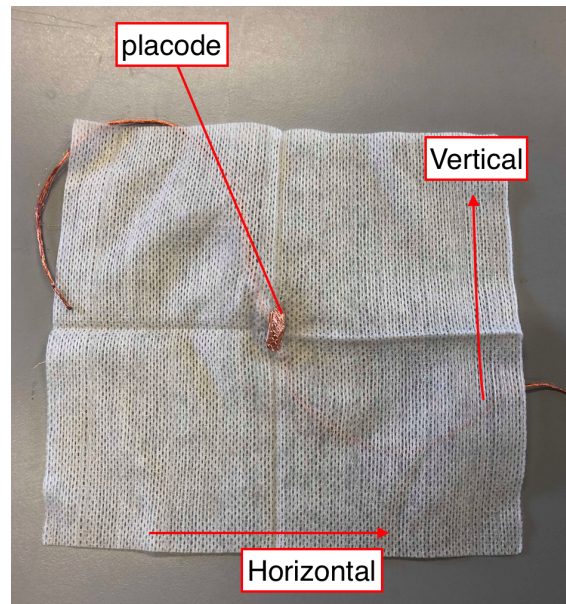


Figure 4.1: Illustration of the different mesh directions.

The first step is to make three different molds, one for each layer. All the molds are made out of polymers (either plexiglas (PMMA) or PETg) so that the Ecoflex™ does not stick to them when cured. For the sake of this explanation, the layers are numbered from one to three from bottom to top.

Secondly, the placode and nerves are to be made. The placode is made out of copper foil tape because it is very thin, bendable and very conductive. This last property is later used to sense possible contact of the surgical instruments with the placode. This is explained more in detail in section 4.2.1. The first step is to fold the foil double on the sticky side of the tape. This is done so that the glue on that side could create an isolating layer between the placode and the nerves. The double folded piece of tape is then cut into an ellipse of 15 x 6 mm. The nerves are made out of silicon wire containing hundreds of tinned copper wires stranded. More specifically, we use 14 AWG (American Wire Gauge) very flexible silicone wire that contains 400 tinned copper wires with a diameter of 0,08 mm. This type of wire is typically used to feed batteries. The silicone coating and very thin wires contained in it allow this wire to be very flexible, a property required for the placode to drop when the surgeon cuts it out of the surface of the defect. The copper wires are bundled together in 7 strands as illustrated on figure 4.2. We use one strand per defect to model the nerves that are attached to the placode. To achieve this, the first step is to remove the silicone coating and take out one strand of wires. Next, the two endings of that strand are tinned, to allow them to pass

through the mesh easily. The placode is then soldered in the middle of the length of the strand of wires. Finally, the endings of the wire are passed through the mesh in the center vertically aligned, close enough together to be completely covered by the placode. On the other side of the mesh, the wires are tied into a simple knot.



Figure 4.2: Example of silicone wire filled with stranded copper wires.

Finally, the different layers have to be made and assembled. Table 4.1 shows the steps to follow to make each layer separately. The wires which model the nerves pass through layer 2 and continue underneath it. When layer 2 cures, the wires will cure with it on the surface and need to be detached from it after the layer is taken out of the mold. When attaching layers 1 and 2 together, these wires will pass between the two. To avoid that the wires stick to the inner surface of the cyst, the wires should be allowed to slack a little bit inside the cyst. Also, to be able to inject liquid into the cyst, a small silicone tube is placed between these 2 layers. The tube is a Silastic RX-50 medical grade tubing.

A very thin layer of Ecoflex™ is applied with a brush or finger on the flat part of layer 2 and then glued to layer 1. Layers 2 and 3 are glued together on the whole surface of layer 3 with a very thin layer of Ecoflex™. When curing, some weights need to be put on the places that are being glued together to avoid air bubbles. When all the layers are attached, the liquid is injected into the cyst with a small syringe. The liquid used is demineralized water.

A picture of the final defect design can be seen in figure 4.4. An exploded view of the final design can be seen on figure 4.5.

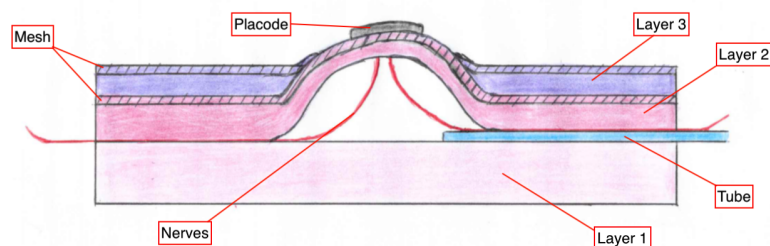
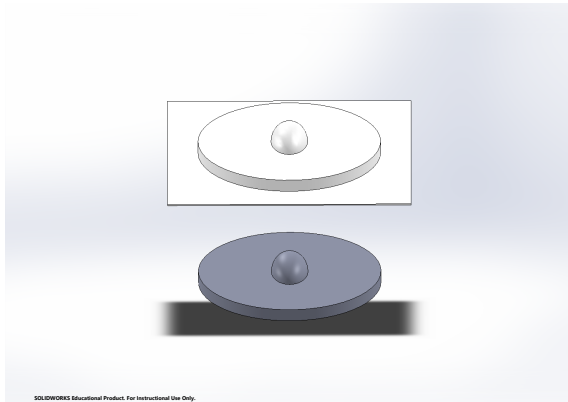
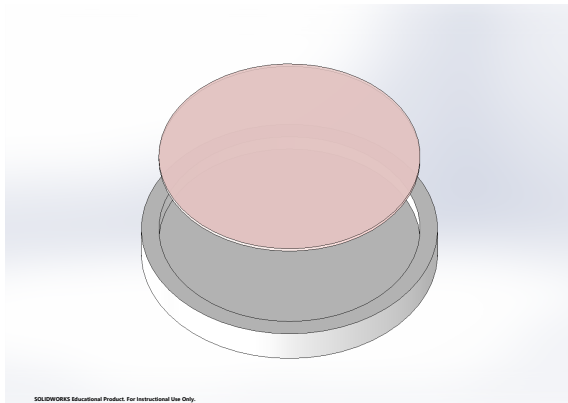


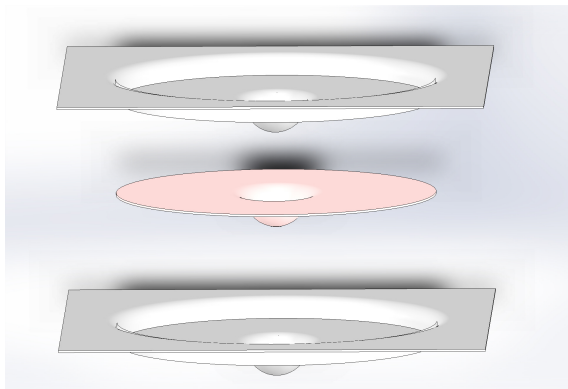
Figure 4.3: Cross-section of the removable defect.



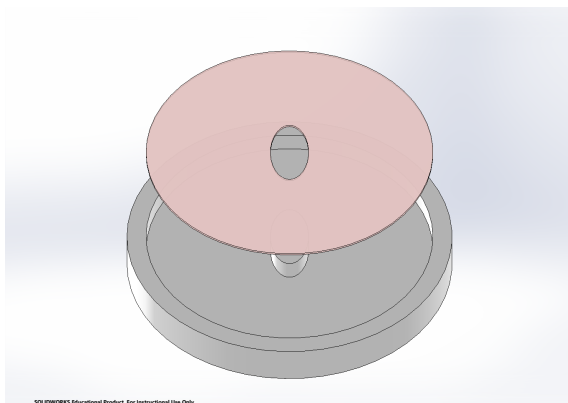
The mold of layer 2 is made by vacuum forming. First a half ellipsoid is 3D printed. A surface finish of 0,1 mm is enough. This piece is then glued in the center of a circular MDF plate with a diameter of 15 cm. The MDF cylinder is laser-cut out of a 6 mm thick MDF plate. A 0,5 mm thick PETg sheet takes the shape of the plate and ellipsoid by vacuum forming it. This mold needs to be made twice.



The first layer is cured in a circular mold with a diameter of 15 cm. The mold is made out of PMMA. The thickness of this layer is not of great importance as it plays no part in the surgery.



Layer 2 is cured in the vacuum formed mold. The first step is to pass the wires, that are soldered to the placode, through the mesh. Then the mesh is placed in the mold with the placode against the polymer on the deepest part of the bulge. Just enough Ecoflex™ is then poured on the mesh to soak it completely but not more. Finally, it is cured between 2 times the same mold with some weights on it to get an even thickness everywhere.



Layer 3 is cured in a similar mold as layer 1. The only difference is the elliptic shaped piece placed in the middle. This piece measures 4 x 2 cm and is laser-cut out of a 8 mm thick PMMA plate. First, the edges of the mesh need to be cut to form a circle that fits perfectly into the mold and the ellipse has to be cut out of the middle of the mesh. Then, 18,2 g of Ecoflex™ is poured into the mold to get a thickness of about 1 mm.

Table 4.1 Steps to make the different layers of the defect.

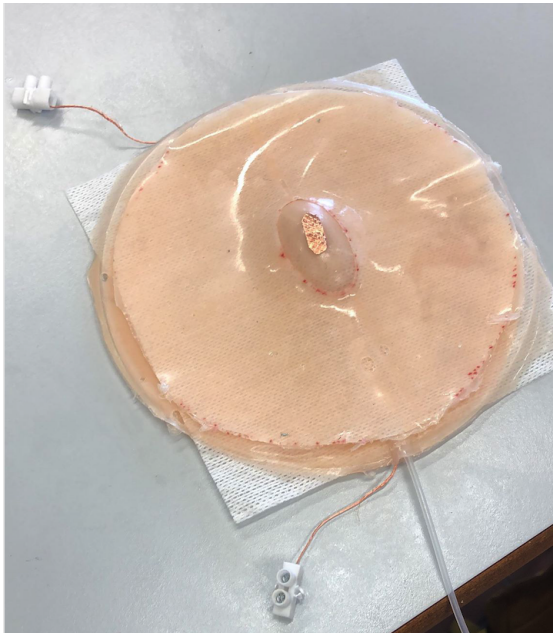


Figure 4.4: Picture of the synthetic defect.

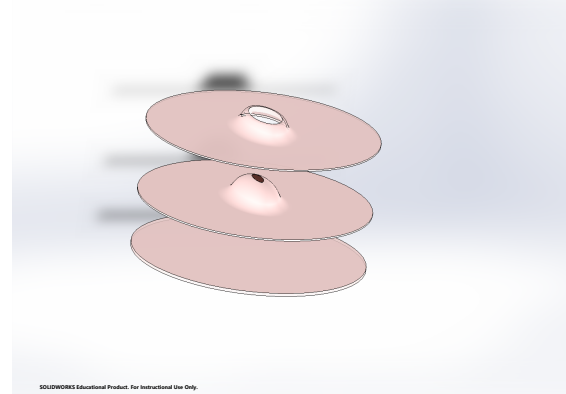


Figure 4.5: Exploded view of the synthetic defect.

As mentioned before, the synthetic defect needs to be replaced after each training. This led to one of the most important requirements for this defect; being as cheap as possible. Table 4.2 shows the price of the different pieces and the total cost for one defect which is 3,38 €. This price only takes the cost of the materials into account and does not incorporate manufacturing costs.

Product	Price (€)	Quantity needed per defect	Price per defect (€)
100 non-sterile non-woven medical compresses, Sylasoft (Company: Sylamed)	1,95	2	0,039
16 m copper foil tape, width 19 mm (Company: 3M)	63,42	0,012 m	0,0476
1 gallon unit Ecoflex™ 00-50 (7,26 kg) (Company: Smooth-On)	176,58	113,8 g	2,768
150 m Silastic RX-50 medical grade tubing	650	12 cm	0,52
24,384 m silicone coated tinned copper wire stranded (Company: bntechgo)	44	1 bundle 30 cm	0,0077
TOTAL			3,38 €

Table 4.2 Price of the removable defect.

4.1.2 Uterine environment

As we deduced from section 3.1, the general shape of the uterine environment was not a defined prerequisite. Therefore, we focused on designing a synthetic environment that is low-cost and functional, while incorporating the important characteristics that were requested:

- Offer the surgeon a distance similar to the real distance from the uterine wall to the defect on the fetal back.
- Offer flexibility in the amount/configuration of incision ports used in the surgery.
- The working area for the surgeon on the outside of the uterus should be similar as in a real life surgery.

To bring these design parameters together, we settled on an open-box design with a pivoting arm ending in a removable synthetic uterine wall. An overview of this design can be seen on figure 4.6. The training model is almost completely made of PMMA. This material allows us to turn CAD

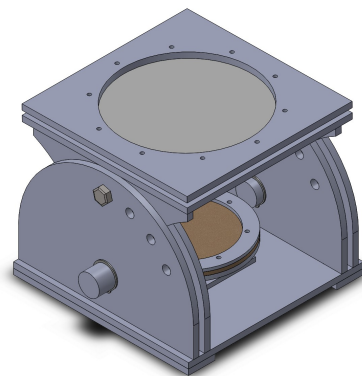


Figure 4.6: An overview of the design of the uterine environment

drawings into a first prototype with ease. We utilized the laser cutter at our local FabLab to create the different parts and used finger joints and acrylate glue to put them together. Another advantage of this material is that it is transparent, which allows surgeons attending a training session to easily follow the progress of the procedure.

4.1.2.1 Synthetic uterine wall

The requirements concerning the working area of the surgeon and the flexibility concerning the placement of incision ports were met through the creation of a removable synthetic uterine wall, shown on figure 4.7. In its essence, it is a circular piece of synthetic material (Ecoflex™ 00-50), measuring 18 centimeters in diameter, with a thickness of six millimeters. The synthetic uterine wall is a simplification of its real counterpart; it is not insufflated (which allows for the open-box design) and secondly, it is isotropic. In reality, the uterine wall is anisotropic and can therefore be

expected to respond differently to forces that the surgeon exerts on it (Mizrahi et al. (1980); Weiss et al. (2006)). The synthetic uterine wall is stretched and fixed in a clamp as shown on figure 4.7.

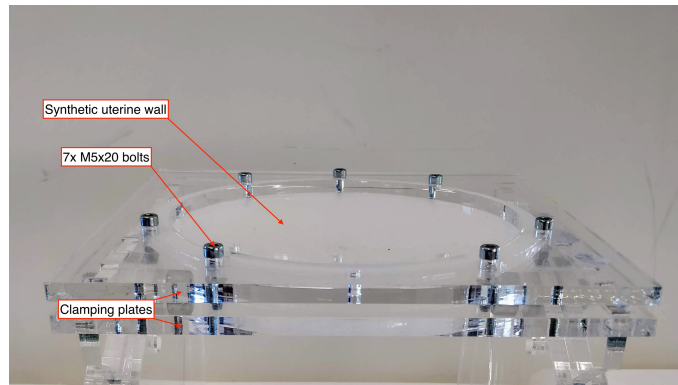


Figure 4.7: The synthetic uterine wall is incorporated into the uterine environment by clamping it in between two square plates.

This clamp consists of two halves that are joined together with seven M5x20 bolts. The two halves of this clamp are square plates with a circular cut-out of 18 centimeters in diameter. This results in the requested similar working area for the surgeon. Due to the clamping design, the synthetic uterine wall can be removed with ease. Because of this, whenever the surgical team wants to perform a training with a different configuration or amount of incision ports, the synthetic uterine wall can be easily replaced by a new version. This offers flexibility in their working approach.

4.1.2.2 Pivoting arms

The requirement that the defect should be located at a distance between 10 and 15 centimeters away from the uterine wall was met by attaching the underside of the clamp containing the synthetic uterine wall to two arms, each measuring 14 centimeters. The arms originate from the bottom part of the training model at approximately the height of the removable defect. Two hinge joints connect the baseplate and the arms, which allows the arms to pivot around said joints. The hinge joints rotate by means of an aluminium shaft with a diameter of 30 mm, held in place by two retaining rings (DIN 471). This effectively allows the uterine wall to be positioned at different angles with respect to the defect. The arms can be attached to their angular guides with an M12 bolt in four predefined positions. Because of this, the arms have four different tilt configurations shown in figure 4.8, ranging from a vertical position to being positioned at a 30° angle with the horizontal.

The hinge joints also allow the arms to be moved out of the way to allow for easier access to the removable defect when it is to be replaced. Because the defect is placed at approximately the height of the shared rotational center of the arms, the distance from the uterine wall to the defect will remain quasi equidistant, regardless of which attachment point is used. Therefore, the distance requirement remains fulfilled. According to our expert, the default position to train the surgery in would be the upright configuration. The aforementioned tilt configurations, however, offers the

possibility to the surgeons to train the surgery at a different approach angle, which may increase its difficulty.

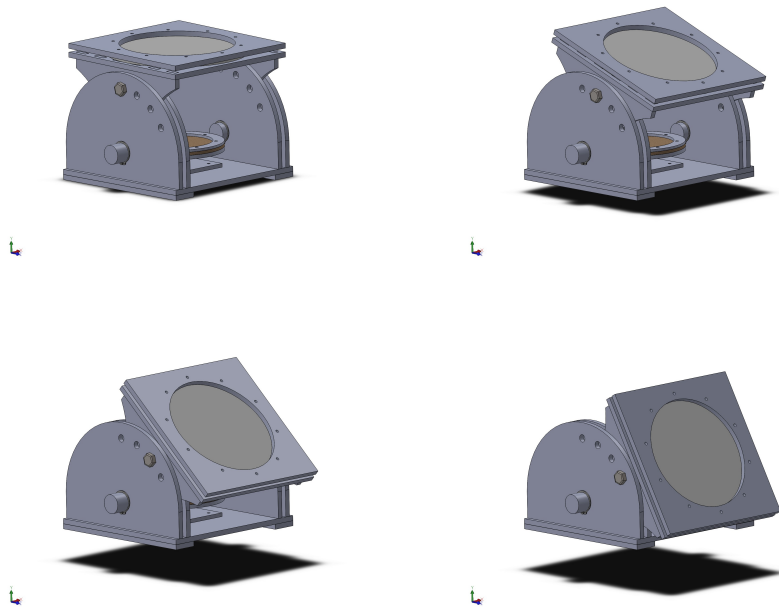


Figure 4.8: The pivoting arm has four attachment points, allowing for four different tilt configurations.

4.1.3 Integration

To attach the removable defect to the uterine environment, several connecting parts are needed. The removable defect is clamped between a circular 8 mm thick PMMA base plate and a 4 mm thick circular ring on the top also made out of PMMA. These plates are joined together by seven M5x25 screws that pass through the defect. The screws are located on a circle with a radius of 6,75 cm. For more stability, the plates can be pressed together with winged nuts. The bottom plate of the defect is mounted onto a force sensor with three M3x10 mm screws. The force sensor itself is attached to a 8 mm thick square plate with three M3x12 mm screws. This is discussed more in detail in section 4.2.3. This "sensor baseplate" connects the removable defect clamp with the connected sensor to the uterine environment and minimizes the amount of times screws have to be removed or inserted into the delicate force sensor. The thicknesses of the different connecting parts are chosen, taking the height of the sensor into account, in such way that the removable defect is approximately at the height of the rotational center of the pivoting arms. The square plate is attached with four M5x20 mm screws and nuts to the base plate of the uterine environment as shown on figure 4.9.

To leave clearance for the nuts of the underneath the baseplate of the uterine environment, it must be elevated. This is achieved by extending the male parts of the finger joints of the uterine environment and to pass through the baseplate into a female support rack on either side. This

creates a clearance of 8 mm under the baseplate. Additionally, three holes of 6 mm in diameter have been made in the uterine environment baseplate to create clearance for the heads of the three M3x10 screws inserted into the force sensor.

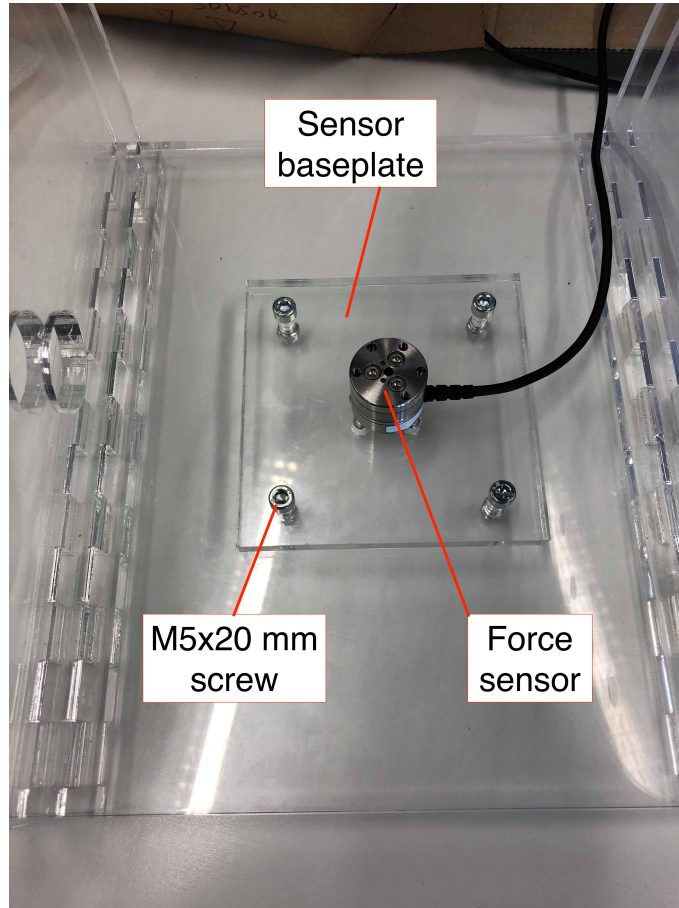


Figure 4.9: The synthetic uterine wall is incorporated into the uterine environment by clamping it in between two square plates.

4.2 Development of a sensing system

In this section, a sensing system is designed to measure the parameters defined in section 3.2 by the use of embedded sensing.

4.2.1 Connectivity

To model the placode on top of the defect, like mentioned before, we use copper foil tape. The nerves that connect the placode to the spinal cord are modelled by naked copper wires that are soldered to the placode. Different wire thicknesses and configurations were tried in order to find one that is flexible enough to allow the placode to drop to the bottom of the defect, back in the spinal canal, when cut out during surgery. The best alternative was found to be the copper con-

tained in silicone coated wire as explained in section 4.1.1. Since the copper wires are tinned, they are conductive along their entire length.

Both the placode and the nerves have to be manipulated with caution since they are potentially still functional. Each manipulation can lead to irreversible trauma to these nervous tissues (Heuer et al. (2014)). In consultation with the medical experts, we came to the conclusion that laparoscopic scissors can cause the most harm to the placode. So, we designed the sensor in a way that as soon as the scissors touch the placode or a nerve, the system registers it. The scissor instrument used during the surgery has to be grounded for the sensor to work.

Figure 4.10 shows the electric scheme of the setup. The dashed line represents the instrument of the surgeon so that part of the scheme is only present when the instrument touches the nerves. The full line with the resistors represents the wire that is embedded in the defect. The signal is measured by a digital port of the Arduino Uno denoted by V_{in} in figure 4.10. From the technical specifications of the Arduino Uno (appendix C), we know that with an operating voltage of 5V, the nominal current per DC pin is 20 mA. Moreover, for the digital pin to report a high input (logical 1) the voltage at the pin should at least be 3V. And to report low, the voltage at the pin should be lower than 1,5V. Using this information, the required resistance values to facilitate this could be computed from (4.1) and (4.3).

When untouched, the wire is under tension and V_{in} is more than 3,5 V which is sensed as a HIGH input by Arduino. As soon as there is a contact between the grounded instrument and the naked copper wire, a short circuit is created, and V_{in} will drop to 0 V which is sensed as LOW by Arduino. The number of times the instrument comes in contact with the nerves or placode is counted and taken as a learning parameter. This number should be as small as possible and decrease after multiple training surgeries.

Since the current at the pin should be around 20 mA, the value of resistance R_1 can be found. The largest current will pass when the instrument touches the wire.

$$I_{pin} = \frac{5V}{R_1} = 20 \text{ mA} \quad (4.1)$$

$$\text{So, } R_1 = 250 \Omega \quad (4.2)$$

The closest default resistance value to 250 Ω , that was available to us, is taken equal to R_1 , so $R_1 = 270 \Omega$.

We now take into account that the voltage at the pin should be at least 3V when the wires are untouched. To avoid any mistake, the value of resistance R_3 is calculated using $V_{in} \geq 3,5 \text{ V}$.

$$V_{in} = \frac{R_3}{R_3 + 274 \Omega} \cdot 5 \text{ V} \geq 3,5 \text{ V} \quad (4.3)$$

$$\text{So, } R_3 \geq 639 \Omega \quad (4.4)$$

The closest default resistance value to 639 Ω , that was available to us, is taken equal to R_3 , so $R_3 = 680 \Omega$.

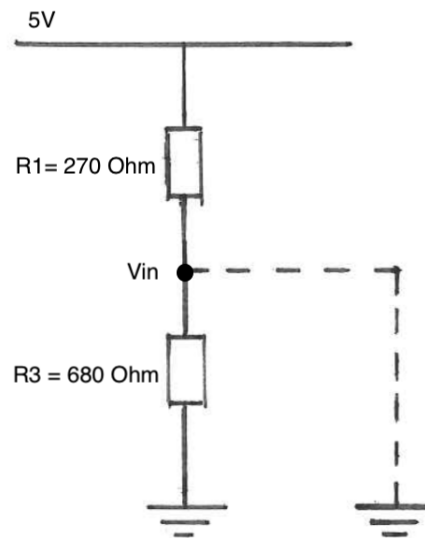


Figure 4.10: Electrical network of setup made to sense contact with spinal nerves

4.2.2 Forces on the uterine wall

While performing the fetoscopic SBA surgery, the uterine wall is deformed due to the manipulations performed by the surgeon on his instruments. This causes the uterine wall to be under tension, which may possibly lead to tissue damage and to iPPROM (Beck et al. (2012)). The goal of this element of the sensing part of the training model is to get an idea of how severely the uterine wall is being affected by the manipulations of the surgeon. This is achieved by tracking the motion of the surgeon's instruments and by computing the forces which the surgeon exerts on the synthetic uterine wall by means of a numerical simulation of that uterine wall.

Since we want the synthetic model to feature a removable synthetic uterine wall, we decided to discard alternatives that incorporate sensors embedded into the uterine wall. One such alternative was the incorporation of embedded flexible sensors, but incorporating these into every recreation of the removable uterine wall was deemed too costly and labor intensive for the production of multiple synthetic uterine walls.

4.2.2.1 Position and orientation tracking

Our chosen approach was to incorporate the Aurora system (by Northern Digital Inc., Canada) in our training model, which was readily available at our engineering department. To track the instruments, we created the setup shown in figure 4.11. In this setup, we attach 6-DOF electromagnetic position sensors of the NDI Aurora system to the handle of each instrument. The system then

captures the position of these instrument handles throughout the surgery. In practice, the 6-DOF position sensors are coils in which a current is induced by an alternating magnetic field produced by the NDI Planar Field Generator (PFG). These induced currents are fed to the NDI System Control Unit (SCU), which in turn reads out position data to the host computer at a sampling rate of 40 Hz (Northern Digital Inc. (2011)). Finally, this position data is further processed using the Robot Operating System (ROS) and a MATLAB program. The PFG serves as the origin for the reference world coordinate system for the position data provided by the SCU.

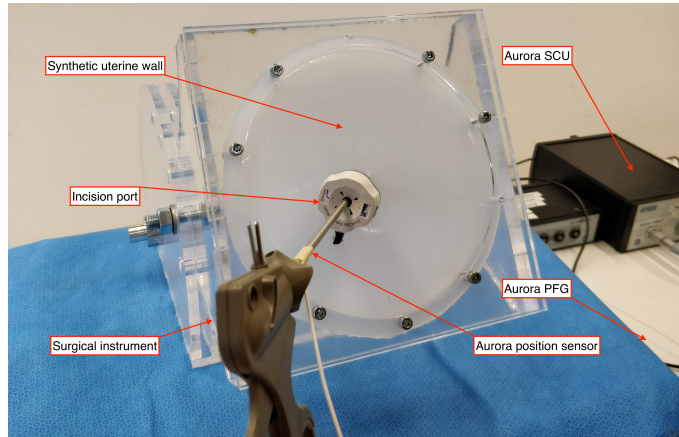


Figure 4.11: Picture of the position tracking setup

4.2.2.2 Instrument motion

The 6-DOF position information of any timestamp, after being processed by the ROS, is given as a position vector \mathbf{p}_{sensor} , containing the coordinates of the sensor with respect to the world coordinate system in the x-, y- and z-direction and as a unit quaternion $\mathbf{q} = (q_r + q_i\mathbf{i} + q_j\mathbf{j} + q_k\mathbf{k})$, expressing the orientation of the sensor. The orientation represented by this quaternion can be written as a matrix rotation (Foley et al. (1990)), using

$$\mathbf{R} = \begin{bmatrix} 1 - 2s(q_j^2 + q_k^2) & 2s(q_iq_j - q_kq_r) & 2s(q_iq_k + q_jq_r) \\ 2s(q_iq_j + q_kq_r) & 1 - 2s(q_i^2 + q_k^2) & 2s(q_jq_k - q_iq_r) \\ 2s(q_iq_k - q_jq_r) & 2s(q_jq_k + q_iq_r) & 1 - 2s(q_i^2 + q_j^2) \end{bmatrix}, \quad (4.5)$$

where $s = 1$ because \mathbf{q} is a unit quaternion. The rotation matrix given by (4.5) can be combined with the position vector \mathbf{p}_{sensor} into a transformation matrix, which represents the position and orientation of a sensor in matrix form for later use.

As mentioned before and as shown in figure 4.11, the motion of the instruments used in the training model is tracked by attaching a sensor solely to the handles of the instruments. The corresponding measurements provide data about the position and orientation of the handles, but not of the full length of the instruments. To evaluate the motion of an instrument, we thus require a fixed relation determining the position of the tip (end) of that instrument with respect to its handle. This can

be achieved by performing a calibration procedure of every instrument before a training session is commenced. During this calibration procedure, two sensors are used to calibrate each instrument, as shown in figure 4.12.

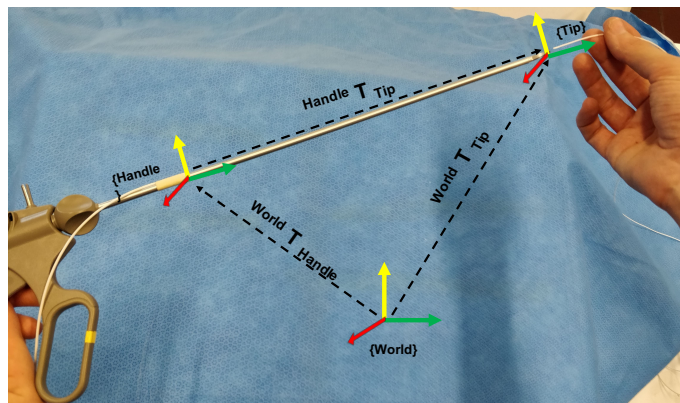


Figure 4.12: The calibration procedure of a surgical instrument is completed by attaching an Aurora sensor to the instrument's handle and by holding a second Aurora sensor at its tip.

One sensor is attached to the handle, while the other one is held at the tip of the instrument. The position data obtained from this procedure can be used to create a transformation matrix for both sensors:

$${}^{World}T_{Handle} \quad \text{and} \quad {}^{World}T_{Tip}$$

This is the matrix representation of the pose and orientation of the handle and the tip respectively. They are expressed relative to world coordinate system placed in the PFG. The aforementioned fixed relation can now be found by using the inverse and multiplicative properties of transformation matrices:

$${}^{Handle}T_{Tip} = ({}^{World}T_{Handle})^{-1} {}^{World}T_{Tip}, \quad (4.6)$$

For every measurement during the training surgery, the 6-DOF position data of the handle sensors can now be used to determine the position of the instrument tips. This yields \mathbf{p}_{inst} , a $M \times 6 \times N$ position array, with M the amount of measurements and N the amount of instruments, with each row containing the coordinates of the handle $(x_{handle}, y_{handle}, z_{handle})$ and tip $(x_{tip}, y_{tip}, z_{tip})$ of an instrument, which together form a line segment representing the position of that instrument at the corresponding measurement.

4.2.2.3 Incision port motion

Intersection of an instrument with the incision plane. As stated before, our goal is to get an idea of how instrument motion is affecting the synthetic uterine wall during the training session. Our approach to achieve this is to process the instruments' motion into motion of their respective incision ports (trocars), which are pierced through the synthetic uterine wall similar to the one shown in figure 4.11. We can use the movements of these incision ports by later incorporating them in our

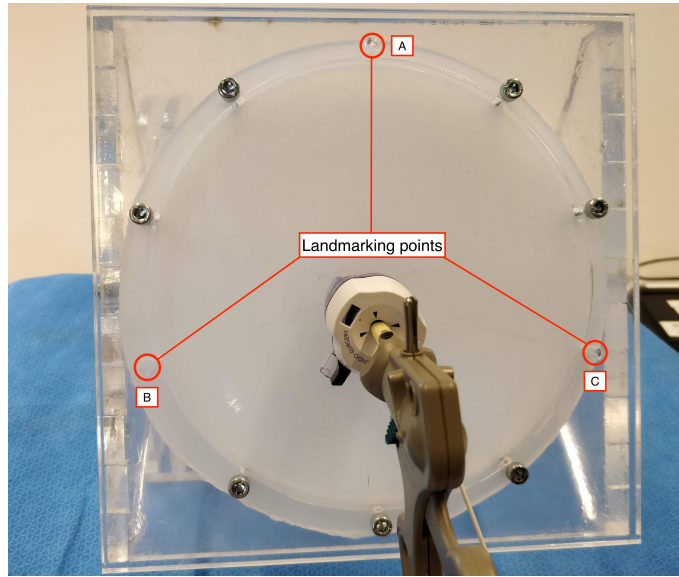


Figure 4.13: The synthetic uterine wall clamp contains three pre-made holes which are used for landmarking the incision plane. To complete the landmarking procedure, these three holes must be touched with the tip of a calibrated instrument. Touching point A stores the location of \mathbf{p}_{planeA} , touching points B and C stores those of \mathbf{p}_{planeB} and \mathbf{p}_{planeC} , respectively.

numerical simulation of the synthetic uterine wall. Our first step to obtain the incision port motion is to create a virtual incision plane, coinciding with the synthetic uterine wall. This can be easily achieved by, in addition to a calibration procedure, performing a landmarking procedure before commencing a training session. In this landmarking procedure, the position of the incision plane is stored by touching three predefined points, annotated in figure 4.13, on the synthetic uterine wall with the tip of a calibrated instrument. Additionally, the calibrated instrument should be inserted into the incision port to store its initial location in order to compute its displacement later on.

During the landmarking procedure, a position sensor is attached to the handle of this instrument. With the fixed relation found in (4.6) between the tip of this instrument and its handle, we can find the coordinates of the three landmarking points relative to the PFG world frame: \mathbf{p}_{planeA} , \mathbf{p}_{planeB} and \mathbf{p}_{planeC} . These are three points that lie in the incision plane. They can be used to calculate the normal vector of the incision plane

$$\mathbf{n}_{plane} = \langle a, b, c \rangle$$

We assume that, for the sake of simplicity, all of the movements of the incision ports happen in-plane with the incision plane. This allows us to compute this motion by simply intersecting the line segments representing the instrument motion, stored in \mathbf{p}_{inst} , with the incision plane, defined by \mathbf{n}_{plane} and a point in the plane \mathbf{p}_{planeA} . For easier interpretation of the steps to find the intersection point between the intersection plane and the aforementioned line segment, figure 4.14 shows the graphical representation of some of the mentioned geometric relations. Suppose the line segment of an instrument at a certain point in time is given by \mathbf{p}_{handle} and \mathbf{p}_{tip} .

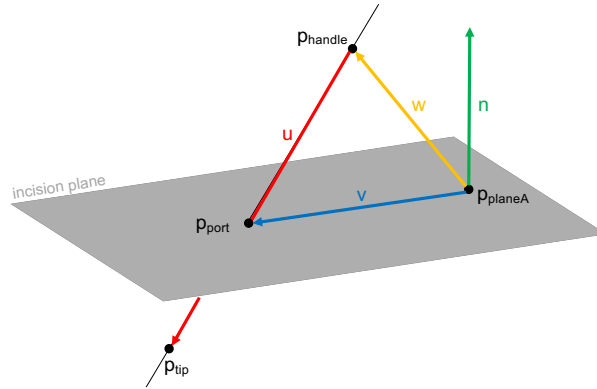


Figure 4.14: Graphical interpretation of the calculations leading up to (4.10). In the case shown on the figure, \mathbf{v} is perpendicular to the normal vector of the plane \mathbf{n} .

The vector \mathbf{u} is a vector representing that line segment.

$$\mathbf{u} = \mathbf{p}_{tip} - \mathbf{p}_{handle} .$$

Using \mathbf{u} , any point along the line \mathbf{p}_{line} containing this line segment can be described by

$$\mathbf{p}_{line} = \mathbf{p}_{handle} + s \mathbf{u} , \quad (4.7)$$

with s a scalar representing the fraction of \mathbf{p}_{line} 's position along the line segment. As an example: if s would be equal to 1, \mathbf{p}_{line} would lie at the position of \mathbf{p}_{tip} . To find the point of intersection between the line segment and the plane, we need to find the value of s corresponding to the position where the line segment intersects with the plane. To achieve this, we first compute the vector \mathbf{w}

$$\mathbf{w} = \mathbf{p}_{planeA} - \mathbf{p}_{handle} .$$

At the point of intersection with the plane, the vector

$$\mathbf{v} = \mathbf{p}_{line} - \mathbf{p}_{planeA} = \mathbf{w} + s \mathbf{u}$$

is perpendicular to the plane's normal vector \mathbf{n} . This is equivalent to stating the dot product condition

$$\langle \mathbf{n}, (\mathbf{w} + s \mathbf{u}) \rangle = 0 . \quad (4.8)$$

To find the value of s , (4.8) can be rewritten as

$$s = \frac{\langle -\mathbf{n}, \mathbf{w} \rangle}{\langle \mathbf{n}, \mathbf{u} \rangle} . \quad (4.9)$$

The value for s found with (4.9) can be used to find the intersection point between the instrument and incision plane:

$$\mathbf{p}_{port} = \mathbf{p}_{handle} + s \mathbf{u} . \quad (4.10)$$

Whenever the value of s lies inside the interval $0 \leq s \leq 1$, there is an intersection between the line segment and the incision plane. In any other case, this intersection point lies outside the line segment. This intersection point can be interpreted as the location of this instrument's incision port (trocar) on the uterine wall at this moment in time.

2D Representation. As we previously assumed that all of the movements of the incision ports are in-plane with the synthetic uterine wall, we can convert the data to 2D to make further processing easier. Additionally, the PFG world coordinate system, which the movements are relative to, does not coincide with the uterine wall. Therefore, we choose to transform the incision port data to use the synthetic wall as a reference. To achieve this, we first compute a set of linearly independent vectors in the incision plane

$$S_{plane1} = \{\mathbf{v}_1, \mathbf{v}_2\}$$

by using the incision plane's normal vector $\mathbf{n}_{plane} = \langle a, b, c \rangle$:

$$\mathbf{v}_1 = \left\langle \frac{b}{a}, -1, 0 \right\rangle \quad \text{and} \quad \mathbf{v}_2 = \left\langle \frac{c}{a}, 0, -1 \right\rangle.$$

Next, we apply the Gram-Schmidt process to turn these vectors into an orthonormal basis of the incision plane. This process works by first creating an orthogonal basis out of the vectors:

$$\mathbf{v}'_2 = \mathbf{v}_2 - \langle \mathbf{v}_1, \mathbf{v}_2 \rangle \mathbf{v}_1. \quad (4.11)$$

This projects \mathbf{v}_2 orthogonally onto the line spanned by \mathbf{v}_1 . The set of vectors

$$S_{plane2} = \{\mathbf{v}_1, \mathbf{v}'_2\}$$

now form an orthogonal basis of the incision plane. This basis is converted into an orthonormal basis by normalizing the base vectors

$$\mathbf{u}_1 = \frac{\mathbf{v}_1}{\|\mathbf{v}_1\|} \quad \text{and} \quad \mathbf{u}_2 = \frac{\mathbf{v}'_2}{\|\mathbf{v}'_2\|},$$

completing the Gram-Schmidt process. We can now convert any computed incision port point \mathbf{p}_{port} , obtained with (4.10), to this basis by a simple matrix multiplication:

$$\mathbf{p}'_{port} = \mathbf{p}_{port} [\mathbf{u}_1 \mathbf{u}_2] \quad (4.12)$$

Finally, we find the center of the synthetic uterine wall $\mathbf{p}_{planeO}(x_0, y_0)$ by using the fact that \mathbf{p}_{planeA} , \mathbf{p}_{planeB} and \mathbf{p}_{planeC} lie on the same circle. We use \mathbf{p}_{planeO} as the origin of the new reference coordinate system and transform the 2D incision port movements computed with (4.12) to have this system as their reference:

$$\mathbf{p}''_{port} = \mathbf{p}'_{port} - \mathbf{p}_{planeO}. \quad (4.13)$$

4.2.2.4 Numerical simulation by means of a spring model

After processing the Aurora data into position data of the incision ports, we want to compute what the forces on the incision ports were at a certain moment during a training session. Additionally, we want to get an idea of how the synthetic uterine wall was deformed at this point in time, giving an indication of the internal stresses in the material. This can be useful information to analyze, for example, a critical step in the surgery or a moment during the surgery in which the largest

movements of the surgeon took place. To determine the behavior of the synthetic uterine wall as a result of the external forces exerted on it by the surgeon, we chose to simulate the uterine wall using a 2D mass spring model (MSM). Simulating soft tissue behavior using MSMs has previously been done before in, for example, surgery training systems and computer graphics (Zhang et al. (2005); Xu et al. (2009); Qiao et al. (2009)). A mass-spring system is a network of point masses m with positions p , interconnected by springs. Some of the masses are fixed in their location, others are not and are free to move around. We want to find the effect of a displacement of one or more points caused on the entire network caused by external force. In our case, we make the decision to solve for a static solution for the sake of simplicity. As we are never looking at solving a dynamic problem, the point masses become obsolete and will thus be left out of consideration. Suppose we have a spring connecting two points \mathbf{p}_a and \mathbf{p}_b . This spring has a resting length L_0 and stiffness k . Whenever the distance between the two points $\|\mathbf{p}_a - \mathbf{p}_b\|$ differs from said resting length, there is a spring force acting on each point, which is equal in magnitude and opposite in direction. This spring force, acting on point \mathbf{p}_a , can be written as

$$\mathbf{F}_{ab} = k (\|\mathbf{p}_a - \mathbf{p}_b\| - L_0) \frac{\mathbf{p}_b - \mathbf{p}_a}{\|\mathbf{p}_a - \mathbf{p}_b\|}. \quad (4.14)$$

In this expression, $k (\|\mathbf{p}_a - \mathbf{p}_b\| - L_0)$ represents the magnitude of the force acting on \mathbf{p}_a and $(\mathbf{p}_b - \mathbf{p}_a)/\|\mathbf{p}_a - \mathbf{p}_b\|$ is a unit vector along the direction in which the force is acting. In a spring network, any one point will have spring connections with multiple other points. For the spring network to be in an equilibrium state, the sum of all forces on every point must equal zero. This includes both spring forces exerted on a point by its neighbors and external forces. The total force acting on a point a can be written as

$$\mathbf{F}_a = \mathbf{F}_{ext} + \sum_{b \in nbrs(a)} \mathbf{F}_{ab} = \mathbf{F}_{ext} + \sum_{b \in nbrs(a)} \left[k (\|\mathbf{p}_a - \mathbf{p}_b\| - L_0) \frac{\mathbf{p}_b - \mathbf{p}_a}{\|\mathbf{p}_a - \mathbf{p}_b\|} \right], \quad (4.15)$$

where $nbrs(a)$ denotes the set of neighbouring points to which point a is connected by a spring. Suppose we have N points in our spring network, each connected to its neighbours via a spring with stiffness k . We can now assemble a force matrix \mathbf{F} of size $N \times 2$, constructed by concatenating the sum of forces on every point of the spring network, found by using (4.15), in the x and y direction. The set of equations that we need to solve to find a static equilibrium, can then be written as

$$\mathbf{F} = \mathbf{0}. \quad (4.16)$$

With (4.16), we now have a general approach on how to construct the set of equilibrium equations for a spring system. Next, we need to discretize our synthetic uterine wall into a spring network so we can apply the general approach to our own spring network.

4.2.2.5 Discretization of the synthetic uterine wall

To discretize the synthetic uterine wall, we need to take into account its size and shape. As seen on figure 4.15, the synthetic uterine wall has a circular shape and is clamped along the outer edge.

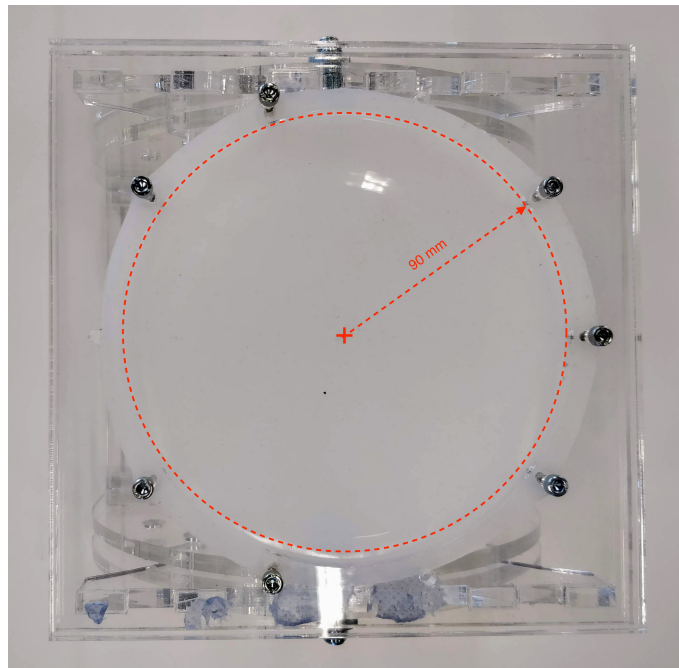


Figure 4.15: The synthetic uterine wall we want to simulate has a circular shape and is clamped along the outer edge.

Additionally, we would like to have nodes in the spring network at the location of the instrument ports. This way, for the sake of simplicity, we can assume external forces are being exerted on the spring network exclusively at these nodes. We chose to discretize the uterine wall by turning it into a mesh of nodes, with the lines connecting the nodes representing springs. As mentioned before in section 4.1.2, the synthetic uterine wall is a simplified, uniform version of its real-life counterpart. Therefore, the mesh representing the uterine wall should desirably be as uniform as possible. To preserve this uniformity in its behavior, we will also assign the same spring constant k to all springs of the spring model. To meet these requirements, we made use of the `distgrid` function (Persson and Strang (2004)), a part of the MATLAB FEATool Multiphysics Toolbox. An additional advantage of this function is that it was designed to be easily adaptable, which makes it easier to improve the quality of the simulation in the future. The general working principle of the `distgrid` function is that its algorithm uses an iterative technique based on the analogy between a mesh and a truss structure, in which the nodes of the mesh are viewed as the joints of the truss structure. The algorithm solves for static equilibrium, considering a force-displacement relation for the bars in the truss. The force displaces the nodes and at each iteration, a Delaunay triangulation algorithm adjusts the topology of the mesh. This yields relatively high quality meshes with a short algorithm. The function's outputs are:

- **p**: the node positions in the final mesh
- **t**: the triangle indices, giving information about which nodes are connected to each other

The notable inputs of the function are:

- `fd`: an implicit distance function, defining the geometry of the mesh
- `bbox`: a bounding box in which the initial node distribution is placed $(x_{min}, y_{min}; x_{max}, y_{max})$
- h_0 : the initial distance between nodes
- `pfixed`: an array of preallocated node positions in the mesh, as desired by the user

To construct the mesh, an initial number of nodes is introduced inside a bounding box defined by the user, separated by h_0 . Of these initial nodes, any nodes that lie outside the geometry (defined by the distance function) are eliminated. Using the aforementioned iterative technique, the algorithm achieves a relatively a uniform mesh structure. In the case of our synthetic uterus wall, we define its circular geometry by the implicit distance function

$$d(x, y) = \sqrt{(x - x_0)^2 + (y - y_0)^2} - R, \quad (4.17)$$

with the circle's center (x_0, y_0) and its radius R . In our case, we choose the center of the circle to be at $(0, 0)$ and its radius to be 90 mm. For our bounding box, we choose a square region coinciding with the boundary of the circle; $(-90, -90; 90, 90)$. The initial length we choose will indirectly decide the size and the amount of nodes of the final mesh as it denotes the spacing between the initial nodes introduced inside our bounding box. Figure 4.16 shows the effect of choosing different values for h_0 , resulting in a finer mesh for smaller values of h_0 . We choose to preallocate one

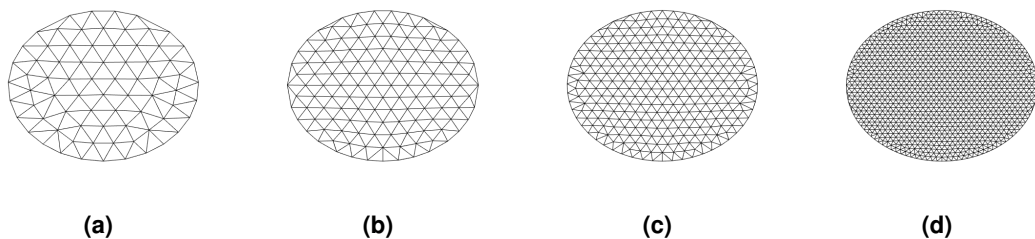


Figure 4.16: Mesh results for a circular geometry (radius = 90 mm) using the distgrid function with a progressively lower value for h_0 : (a) 75 nodes ($h_0 = 20$ mm), (b) 131 nodes ($h_0 = 15$ mm), (c) 295 nodes ($h_0 = 10$ mm), (d) 1177 nodes ($h_0 = 5$ mm)

or more points in the mesh, corresponding with the amount of incision ports in use in the current training session. Figure 4.17, shows a mesh with two preallocated points in blue, as would be the case for a training session with two incision ports. If we compare the quality of this mesh with the one shown in figure 4.16b, we can observe that using the ability of choosing our own node locations, sacrifices some of the uniformity of the mesh.

To figure out the static equilibrium of our spring network, is necessary to determine the neighbor nodes of each node to calculate each spring force using (4.14). We currently have no control over the node numbering process of the distgrid function, which is why we use the triangle indices that it gives as an output to retroactively figure out the neighbors of every node. On figure 4.17, we see the incision port nodes placed in the mesh with their respective neighbour nodes annotated in red.

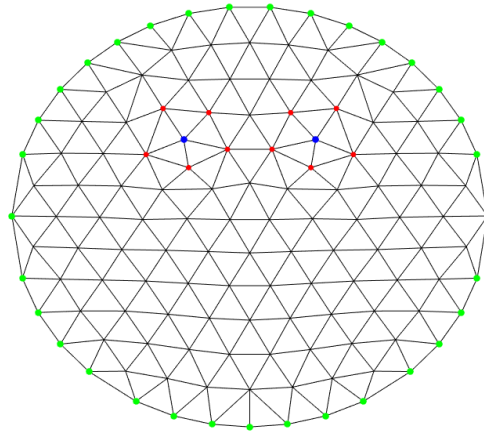


Figure 4.17: Mesh results using two preallocated points, with 133 nodes ($h_0 = 15$ mm): two preallocated points annotated in blue, their neighbouring nodes annotated in red and the boundary nodes annotated in green.

Additionally, it is important to determine the nodes which lie on the outer boundary of the mesh. They are annotated in green. These are the nodes that correspond with the section of the synthetic uterine wall which is clamped along the outer edge, as shown on figure 4.15. These nodes are fixed and cannot move, which is a boundary condition we have to impose in the solver algorithm.

4.2.2.6 Finding a correct static equilibrium

Now that we have an approach to discretize the synthetic uterine wall into a spring network, we want to find a static equilibrium that the network reaches after being affected by one or more external forces \mathbf{F}_{ext} . In our case, we know the correct position of one or more nodes of the network, because of the measurements with the Aurora system, and the value for \mathbf{F}_{ext} is unknown. To achieve this, our approach is to make an initial guess for \mathbf{F}_{ext} and compute a static equilibrium of the spring network for this \mathbf{F}_{ext} .

Solver procedure. This static equilibrium is found by first computing (4.14) for every spring in the network and subsequently computing (4.15) for every node in the network. To ensure every spring force is calculated only once, the algorithm runs through all the nodes of the network in an ascending order, but only calculates the spring force between respective nodes a and b while the condition

$$a < b$$

is satisfied. For this, we make use of the fact that $\mathbf{F}_{ab} = -\mathbf{F}_{ba}$. Using the function `fsolve`, a part of the MATLAB Optimization Toolbox, a static equilibrium of the network is then found. An example of

such a static equilibrium is shown in figure 4.18. On figure 4.18a, the uterine wall is shown without any deformation. Two preallocated nodes have been assigned at symmetrical locations from the circle center. Next, we apply an external force of -1 N along the x-axis to the left node and one of 1 N along the axis to the right node. The resulting deformation is shown in figure 4.18b, indicated by a color value representing the relative displacement of each point of the uterine wall. The maximal deformation is found in the nodes onto which the force was exerted and is computed to be equal to 12,954 mm in both nodes. The equal deformation is to be expected because of the symmetrical node layout and application of force.

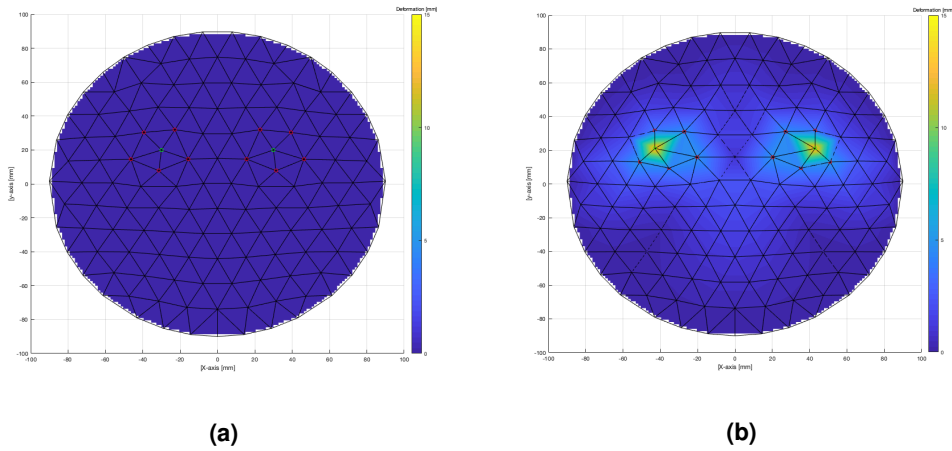


Figure 4.18: A static equilibrium of a spring model ($h_0 = 15 \text{ mm}$, $N = 133$, $k = 60 \text{ N/m}$) with two preallocated nodes found after applying a force of -1 N along the x-axis to the left preallocated node and a force of 1 N along the axis to the right preallocated node.

Fsolve, being a 'Newtonian-esque' optimization method, will calculate the Jacobian of the force matrix in every iteration. To speed up the computation time and improve the accuracy of the solution it converges upon, we provide fsolve with a predefined Jacobian:

$$J[\mathbf{F}] = \begin{bmatrix} J_1 & J_{12} & \cdots & J_{1N} \\ J_{12} & J_2 & \cdots & J_{2N} \\ \vdots & \vdots & \ddots & \vdots \\ J_{N1} & J_{2N} & \cdots & J_N \end{bmatrix}, \quad (4.18)$$

where every element is a $[2 \times 2]$ submatrix, which makes $J[\mathbf{F}]$ a $[2N \times 2N]$ matrix, with N being the amount of nodes in the spring network. The elements on the diagonal are the aggregate of the submatrices relating to every spring force acting on the corresponding node. For example, if node 2 is connected to nodes 1 and 3, the diagonal submatrix J_2 will be

$$J_2 = -J_{21} - J_{23}. \quad (4.19)$$

The Jacobian of any spring force \mathbf{F}_{ab} can be calculated by computing

$$J_{ab} = \frac{\partial \mathbf{F}_{ab}}{\partial \mathbf{p}_b}, \quad (4.20)$$

which can be interpreted as the rate of change of the spring force acting on nodes a and b (given by (4.14)) due to the change in position of node b . This derivative can be written as

$$\frac{\partial \mathbf{F}_{ab}}{\partial \mathbf{p}_b} = kI - kL_0 \frac{\|\mathbf{d}_{ab}\|^2 I - \mathbf{d}_{ab} \mathbf{d}_{ab}^T}{\|\mathbf{d}_{ab}\|^3}, \quad (4.21)$$

where I is a $[2 \times 2]$ identity matrix and \mathbf{d}_{ab} denotes the distance between node a and b . Because any sign changes are canceled out, we can observe that $J_{ab} = J_{ba}$.

Imposing boundary conditions. As mentioned before, a boundary condition must be imposed on the fixed nodes (shown in figure 4.17) to make sure their positions remain unchanged. This is done in two steps. First, the forces on the boundary nodes are set to zero instead of being calculated by (4.15). Secondly, we replace the columns and rows of the boundary nodes in $J[\mathbf{F}]$ by the respective elements of the identity matrix of size $[2N \times 2N]$. This way, the movements of other nodes will have no effect on them.

Error calculation. After `fsolve` converges on a solution for the node positions of the spring network, these positions are checked by comparing them to the correct (measured) positions. Suppose the training session used three ports, of which the positions were computed by processing the Aurora data via the aforementioned process. This means we know the correct position of node 1, 2 and 3. To compare these correct positions with the positions computed by `fsolve`, we create the error vector

$$\boldsymbol{\varepsilon}_{pos} = \begin{vmatrix} \mathbf{p}_1 & - & \mathbf{p}'_1 \\ \mathbf{p}_2 & - & \mathbf{p}'_2 \\ \mathbf{p}_3 & - & \mathbf{p}'_3 \end{vmatrix}. \quad (4.22)$$

The value of $\boldsymbol{\varepsilon}_{pos}$ can be minimized by an outlying optimization function by iteratively making a new guess for the external force \mathbf{F}_{ext} . Unfortunately, we did not manage to construct this outlying optimization function, which is why we discuss it in section 6.2. However, to report completed work, we will discuss our efforts to calibrate the spring model in the next section.

4.2.2.7 Calibration of spring model

In section 4.2.2.4 to 4.2.2.6, we attempted to create a numerical simulation to model the behavior of the synthetic uterine wall. As mentioned before, this numerical simulation would estimate the forces exerted on the synthetic uterine wall by the incision ports. At the same time, it would also determine how the entire uterine wall deforms due to those forces. This numerical simulation must be calibrated by means of real-world values; real forces relating to a certain displacement of the synthetic uterine wall. The purpose of this calibration procedure is to adjust the numerical simulation in a way that it produces results that correspond to reality. There are two ways to adjust the numerical simulation so that it can be calibrated. With the current model we can adjust

- the topology of the mesh; we can make it finer or coarser by adapting the value of h_0 .
- the spring constant k of the springs.

By adjusting these two parameters, we can obtain different results from the numerical simulation. To get an indication of the influence of these parameters, we create a test spring model with a preallocated node at the center of the network, shown in figure 4.19.

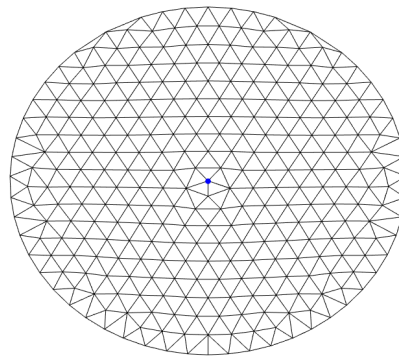


Figure 4.19: A test spring model with a preallocated node at the center.

We now exert a force of 1 N along the x axis on this node and measure the displacement of the node with respect to its starting location. To compute the influence of the aforementioned parameters on the spring model, we run different combinations of values of h_0 and k and compute the displacement of the preallocated node every time. The result of this is shown in figure 4.20.

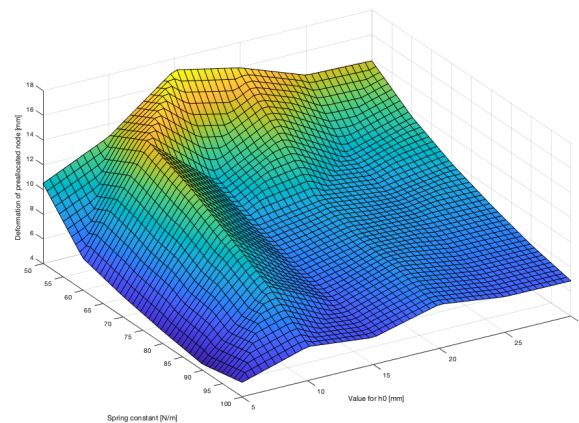


Figure 4.20: The influence of the h_0 and k parameters on the displacement of a node in the spring network after being affected by a force of 1 N.

Preparation of calibration experiment To perform measurements for the calibration of our spring model, we used an instrument developed by Nele Troonbeeckx, a colleague of ours at the mechanical engineering department of KU Leuven. She designed a beam equipped with strain gauges arranged in two half bridge configurations at two different sites on the beam, shown in figure 4.21. Both half bridges are laid out in the longitudinal direction of the beam and measure tensile and

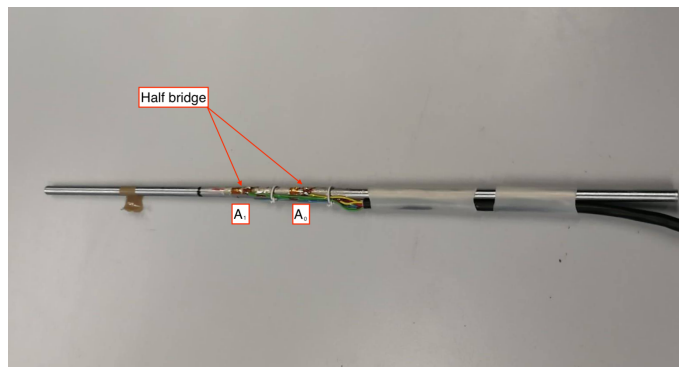


Figure 4.21: A photo of the instrument developed by Nele Troonbeeckx.

compressive strain. Hence, they can only be used to measure forces and moments that cause bending stress. By placing this instrument through the synthetic uterine wall and measuring the force and moment on the instrument (by using the half bridges), we can compute the forces that are being exerted on the synthetic uterine wall. An illustration of this loading case exerted on the instrument is given in figure 4.22.

As mentioned before, the instrument contains two strain gauge half bridges, A_0 and A_1 , as shown on figure 4.22. These strain gauges measure the difference in elongation of the beam at the site where they are attached, denoted by ε_0 and ε_1 respectively. To be able to measure the forces and bending moments on the instrument, we need to construct a relation that convert these strains

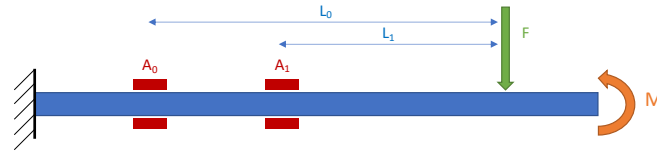


Figure 4.22: An illustration of the instrument developed by Nele Troonbeeckx.

into the bending moment and/or force that caused them. To achieve this, we apply the principle of superposition to the loading case illustrated in figure 4.22:

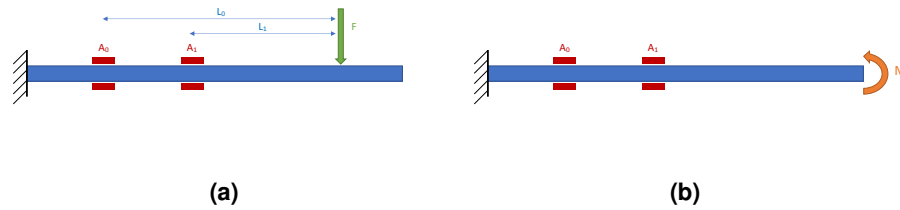


Figure 4.23: The loading case of figure 4.22 split up into a case of pure force and pure moment loading.

The strain gauges at the top of the beam in 4.23a are under tensile stress due to the bending moment at each strain gauge caused by the force F , which acts on the beam at a distance of L_0 from half bridge A_0 and L_1 from A_1 . These strains measured by the half bridges in this pure force case are denoted by ε_{0F} and ε_{1F} , respectively. The bending moments experienced by the strain gauges can be written as:

$$M_{0F} = F L_0 \quad \text{and} \quad M_{1F} = F L_1$$

The strain gauges at the top of the beam in figure 4.23b are under compressive stress due to the bending moment M , which has the same magnitude over the entire length of the beam. The strains measured by the half bridges A_0 and A_1 in this pure moment case are denoted by ε_{0M} and ε_{1M} , respectively. To equate the strains measured by the half bridges due to the bending moments in these cases, we factor in the constants C_1 and C_2 for the pure force case

$$\varepsilon_{0F} = C_1 M_{0F} = C_1 F L_0 \quad \text{and} \quad \varepsilon_{1F} = C_2 M_{1F} = C_2 F L_1, \quad (4.23)$$

and C_3 and C_4 for the pure moment case

$$\varepsilon_{0M} = C_3 M \quad \text{and} \quad \varepsilon_{1M} = C_4 M. \quad (4.24)$$

In the combined loading case, the strain gauges each measure a value that can be written as a combination of the above strains:

$$\varepsilon_0 = \varepsilon_{0F} + \varepsilon_{0M} \quad \text{and} \quad \varepsilon_1 = \varepsilon_{1F} + \varepsilon_{1M} \quad (4.25)$$

The relations in (4.23) can be rearranged into

$$\frac{C_1 \varepsilon_{0F}}{L_0} = \frac{C_2 \varepsilon_{1F}}{L_1}. \quad (4.26)$$

Similarly, the relations in (4.24) can be rearranged into

$$C_3 \varepsilon_{0M} = C_4 \varepsilon_{1M}. \quad (4.27)$$

Combined with (4.25), the above relations can be used to construct a calibration matrix of the force sensing instrument:

$$\begin{bmatrix} \frac{C_1}{L_0} & 0 & \frac{-C_2}{L_1} & 0 \\ 0 & C_3 & 0 & -C_4 \\ 1 & 1 & 0 & 0 \\ 0 & 0 & 1 & 1 \end{bmatrix} \begin{bmatrix} \varepsilon_{0F} \\ \varepsilon_{0M} \\ \varepsilon_{1F} \\ \varepsilon_{1M} \end{bmatrix} = \begin{bmatrix} 0 \\ 0 \\ \varepsilon_0 \\ \varepsilon_1 \end{bmatrix}. \quad (4.28)$$

The value of C_1 , C_2 , C_3 and C_4 can be found empirically by performing calibration experiments; measuring ε_0 and ε_1 in response to a pure force and in response to a pure moment. The pure force experiment was performed by clamping the instrument on one end and attaching a premeasured weight at the other, as shown on figure 4.24. The measurements of the half bridges were read by a field-programmable gate array (FPGA) (NI cRIO-9074, National Instruments, United States) and processed with a LabView program supplied to us by our colleague Nele Troonbeeckx.

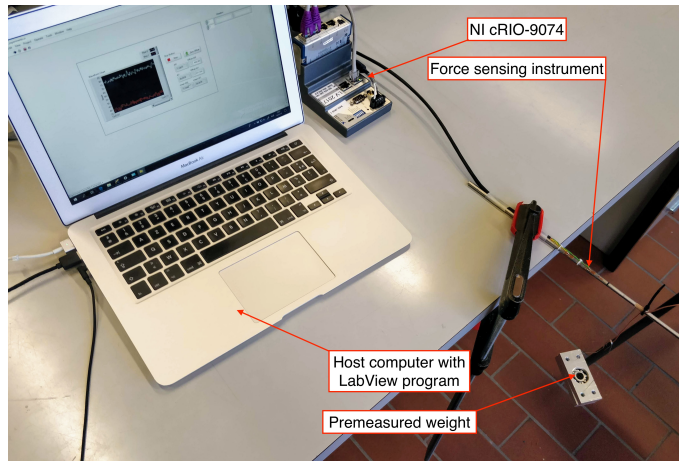


Figure 4.24: The set-up of the pure force experiment to calibrate the force sensing instrument.

The premeasured weight was attached at a distance of L_0 away from half bridge A_0 and L_1 away from A_1 . The experiment was repeated five times, each time with a larger premeasured weight. The bending moment caused by these weights is given by

$$M_F = m g L, \quad (4.29)$$

with L measuring 9,73 cm for A_0 and 6,73 cm for A_1 . This yields the linear relation between bending moment and strain, shown in figure 4.25. A linear relation is to be expected, as the loads

acting on the instrument should leave it well within the region of elastic deformation (so $\sigma \propto \varepsilon$). The slopes of the linear relations are the constants C_1 and C_2 , respectively converting the strains measured in A_0 and A_1 to the bending moment that caused them. We find $C_1 = C_2 = 0,0017 \text{ Nm}/\mu\text{strain}$.

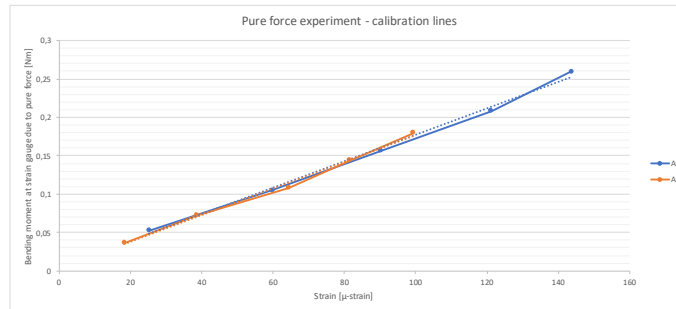


Figure 4.25: The results of exerting pure force on the force sensing instrument

The pure moment measurement was performed by clamping the instrument on one end and applying a bending moment on it. The bending moment was applied by attaching a known weight to a rod attached to the instrument, a distance d away from the instrument's centerline, as illustrated in figure 4.26.

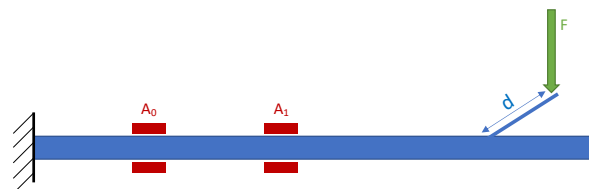


Figure 4.26: An illustration of the pure moment experiment to calibrate the force sensing instrument.

The experiment was repeated four times, each time with a larger premeasured weight. The bending moment caused by these weights is given by (4.29), with L being the distance d in this case, measuring 6,7 cm. We oriented the instrument in a way that the strain gauges would measure a positive (counterclockwise convention) bending moment. This yields the linear relation between bending moment and strain, shown in figure 4.27. Similar to the previous case, the slopes of these linear relations are the constants C_3 and C_4 . We find $C_3 = -0,0015$ and $C_4 = -0,0016 \text{ Nm}/\mu\text{strain}$. The negative values of these slopes indicate that the strain gauges measured compressive strain. For this reason, our calibration computes a positive moment when the half bridges measure a negative strain.

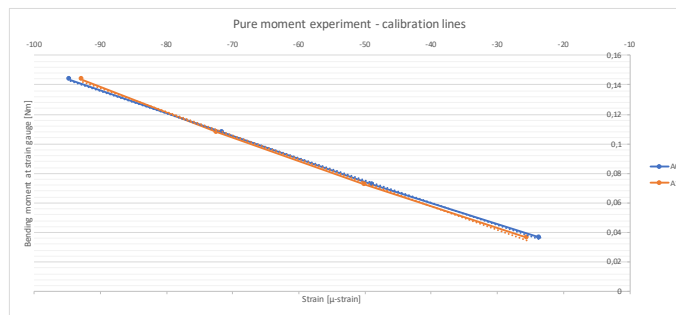


Figure 4.27: The results of exerting pure moment on the force sensing instrument

With C_1 , C_2 , C_3 and C_4 found, we can use (4.28) to convert measured strains in A_0 and A_1 to a corresponding bending moment and/or force.

Spring model calibration experiment To make the behavior of the numerical synthetic uterine wall representative of the behavior of its real-life counterpart, it must be calibrated with displacement and external force measurements. As mentioned before in section 4.1.2.1, we simplified the synthetic uterine wall to be isotropic. Therefore, we can assume that it exhibits the same behavior axisymmetrically. This allows us to perform force measurements in only one direction and extrapolate them to the entire synthetic uterine wall. The calibrated force sensing instrument can be used to measure the forces and moments it experiences in one plane of motion. By at the same time measuring the position of the incision point, we know how a known point of the uterine wall displaces in response to a force. We can subsequently use this information to calibrate the spring model.

To measure the forces and moments experienced by the instrument and the position of its incision point in the synthetic uterine wall simultaneously, we constructed the experimental setup shown in figure 4.28.

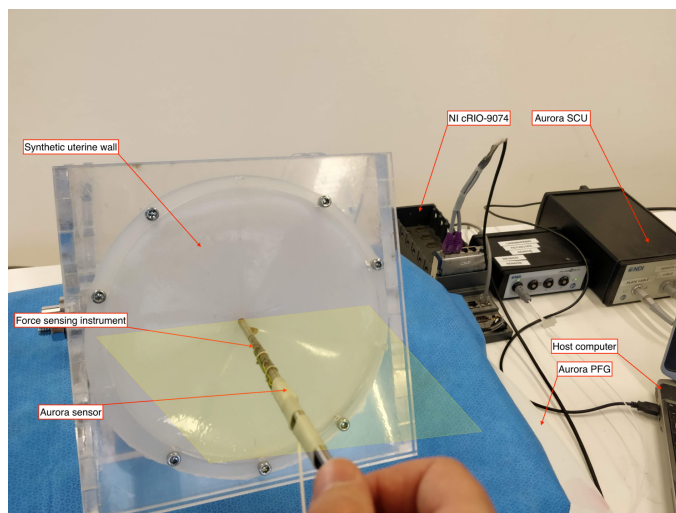


Figure 4.28: The set-up of the spring model calibration experiment.

During the experiment, the operator performed movements in one plane of motion, illustrated by the yellow plane. Every movement was intended to be a rotational movement but contained an involuntary translational portion. The movements were constrained solely by the intersection with the synthetic uterine wall. During the experiment, strains due to the forces and moments exerted on the instrument were measured with an FPGA (NI cRIO-9074) and processed with the aforementioned LabView program. The same distance used in the calibration measurements was used to measure the force at the outer layer of the synthetic uterine wall. Simultaneously, the position and orientation of the handle of the instrument was tracked by an Aurora sensor, the Aurora PFG, SCU and the host computer. By using our MATLAB program, the motion of the incision point was computed based on this data. In the course of one measurement, the operator would start the motion tracking software, perform a movement and hold. At this moment, he would capture strain data. In figure 4.29 the position measurements of the incision point of a movement towards the left are shown.

Figure 4.30 shows the strain measurements and the corresponding computed force and moments

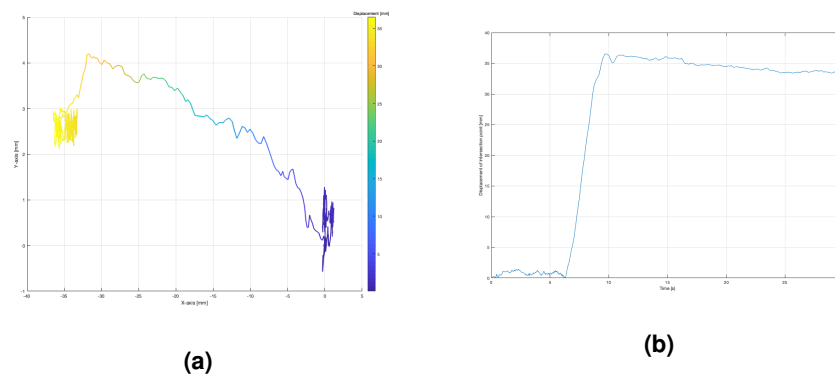


Figure 4.29: The trajectory and absolute displacement of the incision point caused by the operator moving to the left.

for the portion of this movement where the instrument is held after the movement to the left is completed.

As there were no absolute timestamps recorded for the measurements of the force sensitive instrument, the data required manual syncing, which will undoubtedly have caused inaccuracies in the dataset we ended up with to calibrate the spring model. The fluctuations in force and moment are most likely caused by tremor of the operator's hand. This was a phenomenon seen in all measurements and increased with deformation. In this measurement, we expect the moment affecting the instrument to be positive. Because of this, we assume that moments that fluctuate to a negative value are caused by the aforementioned tremor and are thus discarded. To construct the dataset for the spring model calibration, we selected a couple of maximum moment - force per measurement. The measured force exerted on the instrument can originate from two sources. First, if the pivot point of the rotational movement is exactly at the middle of the thickness of the synthetic uterine wall, the counteracting forces due to the bending moment cancel out at each outer end of the wall. However, if the pivot point is off-center, there is a resulting lateral force F_r due the rotational move-

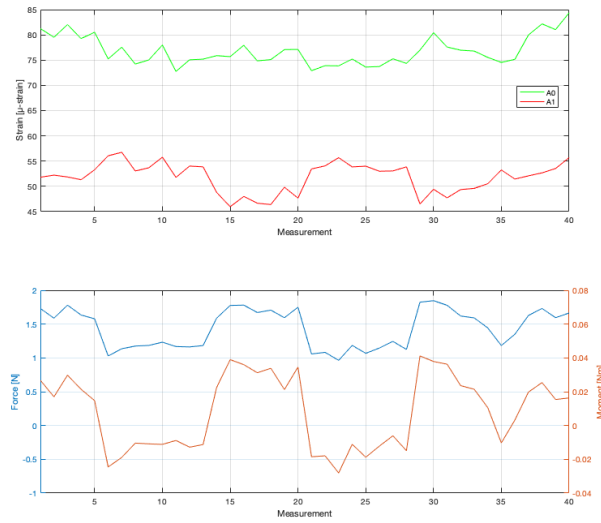


Figure 4.30: Strain measurements taken with the force sensitive instrument for a portion of the trajectory shown in figure 4.29 and the corresponding computed forces and moments.

ment, in addition to the moment (Javaux et al. (2016)). Second, as mentioned before the operator's movements were not limited to solely rotational movement. As a result, the force measurement can also contain lateral force due to the translational portion of the instrument motion. In other words, this implies that the measurements of the force at the outer layer of the synthetic uterine wall may contain a lateral force not caused by the rotational motion.

Estimating the location of the pivot point of the instrument is out of the scope of this thesis. As a consequence, we cannot correctly figure out what the effect of the moment is on the outer edges of the synthetic uterine wall; the lever arm of the moment is unknown. However, as a simplification, we assume that the pivot point is at the middle of the thickness of the synthetic uterine wall. This allows us to, despite not knowing the pivot point, incorporate some measure of the internal force at the outer layer of the uterine wall as an effect of the bending moment. The bending moments during the experiment measured 0,04 Nm maximally, which is a fraction of the interaction torques measured in (Javaux et al. (2016)). This is to be expected, as the thickness of the abdominal wall used in their experiment was more than six times the thickness of our synthetic uterine wall. Because of this, we hypothesize that our pivot point assumption will have a limited contribution to the total force at the outer layer.

The contribution of the measured bending moment $M_{measured}$ to the measured force at the outer layer of the synthetic uterine wall is calculated by using its lever arm to that outer layer, which measures 3 mm due to our assumption:

$$F_{moment} = \frac{M_{measured}}{t/2} \quad (4.30)$$

By combining the force contribution of the bending moment with the measured lateral force, a total force on the outer layer of the synthetic uterine wall can be calculated. This lateral force can

then be connected to a displacement of the incision point for the corresponding movement. Figure 4.31 shows the computed results from the calibration experiment. Where one would expect an increase in force with an increase in incision port displacement, the results are scattered illogically. This indicates that the computation of the results came short or the experiment was performed inadequately.

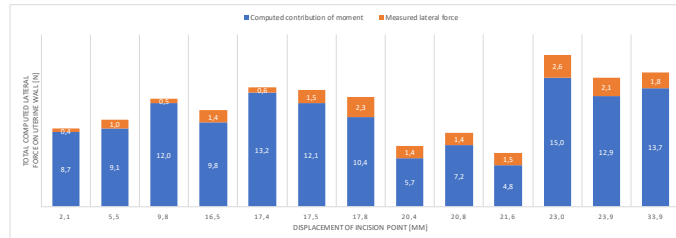


Figure 4.31: Computed measurements from the calibration experiment with the force sensitive instrument

The quality of the force measurements is inadequate, which can thus not be used to calibrate the spring model which, as mentioned at the end of section 4.2.2.6, is not yet able to completely converge onto a correct solution. Possible improvements to the procedure of the calibration experiment are discussed in section 6.2.

4.2.3 Forces on fetus

The final parameter we want to measure are the forces applied on the fetus during surgery. For that we use the 6-DOF force and torque sensor nano25 with metric calibration SI 125-03 from the company ATI Industrial automation. The ranges and resolutions, specifications and drawing of the sensor can be found in appendix D. The sensor is also used to determine where the forces are applied.

The sensor is fragile and should be manipulated with care. On the drawings, it is explicitly stated that the attachment screws should not exceed the depth of the holes. Since the bottom of the defect clamp is 8 mm thick and the holes of the sensor are 3,5 mm deep and have a diameter of 3 mm, we use M3x10 mm screws. The same goes for the bottom holes of the sensor that need to be attached to the square plate. This plate is 8 mm thick and the depth of the screw holes of the sensor are 7,5 mm so we use 3x12 mm screws. The screws are inserted with an adjustable torque screwdriver to ensure that the torque exerted is restricted. The screwdriver is set on the lowest torque setting, which is 15 cNm. It is also important to keep the ranges of the forces and torques in mind and not exceed them to preserve the sensor, even though short overloads are allowed.

Figure 4.32 shows the set-up we used to process the data coming from the sensor. To be able to compute the data from the sensor, the signal first has first to be sampled through data acquisition. Instead of using a USB data acquisition device as shown on the figure, we use a Beckhoff Bus terminal system (EtherCAT (Ethernet for Control Automation Technology)) that is connected to the computer with an ethernet cable. The load information coming from the transducer is processed in

the Orocos framework that runs on Linux. The forces and torques are gathered from the sensor at a rate of 60 Hz and are divided into seven columns. In order, these columns are: time stamp, force F_x , force F_y , force F_z , torque T_x , torque T_y and torque T_z . Figure 4.33 shows the direction of those forces and torques. As can be seen on figure 4.34, the bottom clamp of the defect is attached to the sensor in such a way that there is a screw hole on the positive x-axis. The black square on the right of this figure represents the feeding cable of the transducer, which is in the positive x direction as can be seen on the technical drawings of the sensor in appendix D.

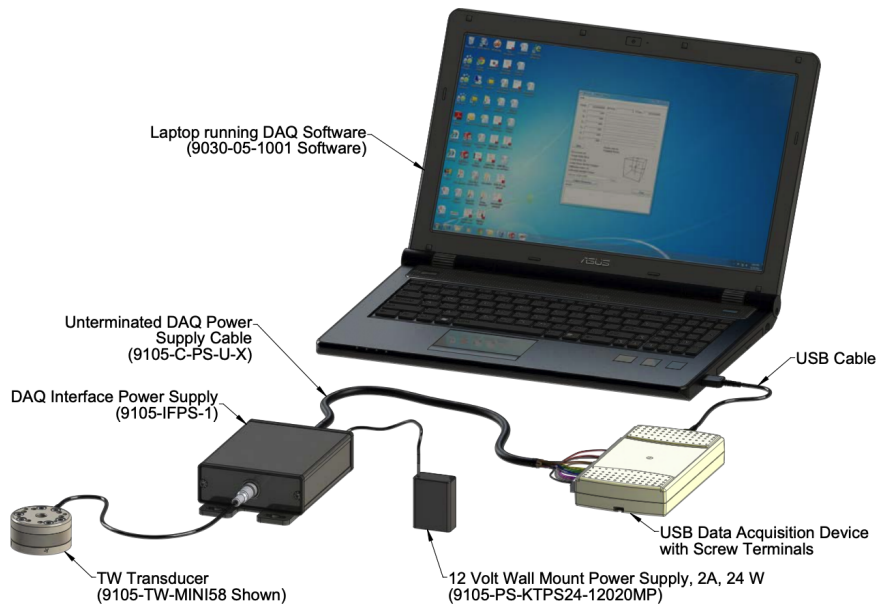


Figure 4.32: Set-up for the recording of data from the force and torque sensor.

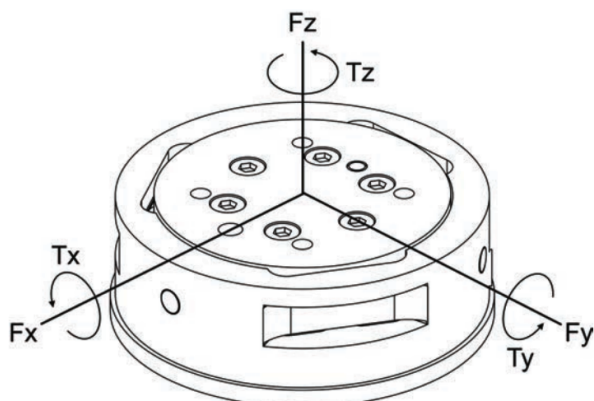


Figure 4.33: Illustration of forces and torques directions.

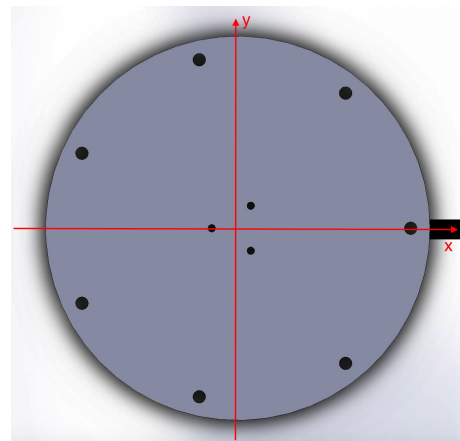


Figure 4.34: Orientation of defect with respect to coordinates of the sensor.

The data first had to be calibrated for our set-up and application. When the defect is attached to

the sensor but no external force is applied to it, there was a force in the negative z-direction due to the weight of the defect and clamp. Additionally, the other components contained a non-zero offset. This offset can be due to noise or the table not being entirely horizontal. The averages of these initial values were subtracted from the measurements to get the real values. Each training surgery should start a recording before touching the defect so that this offset can be determined.

Next, some tests were done to check if the forces and torques correspond to the real ones. This was done by placing four known weights on several known locations. More specifically, we placed weights of 138 g, 180 g, 709 g and 1272 g on the screw located on the x-axis and on the third screw counterclockwise from the x-axis. The average error on F_z is equal to 0,23 N. The average error on T_y is 0,33 Nm and on T_x it is equal to 0,28 Nm. Moreover, as can be seen on figure 4.35, these outputs of the sensor vary linearly with increasing load.

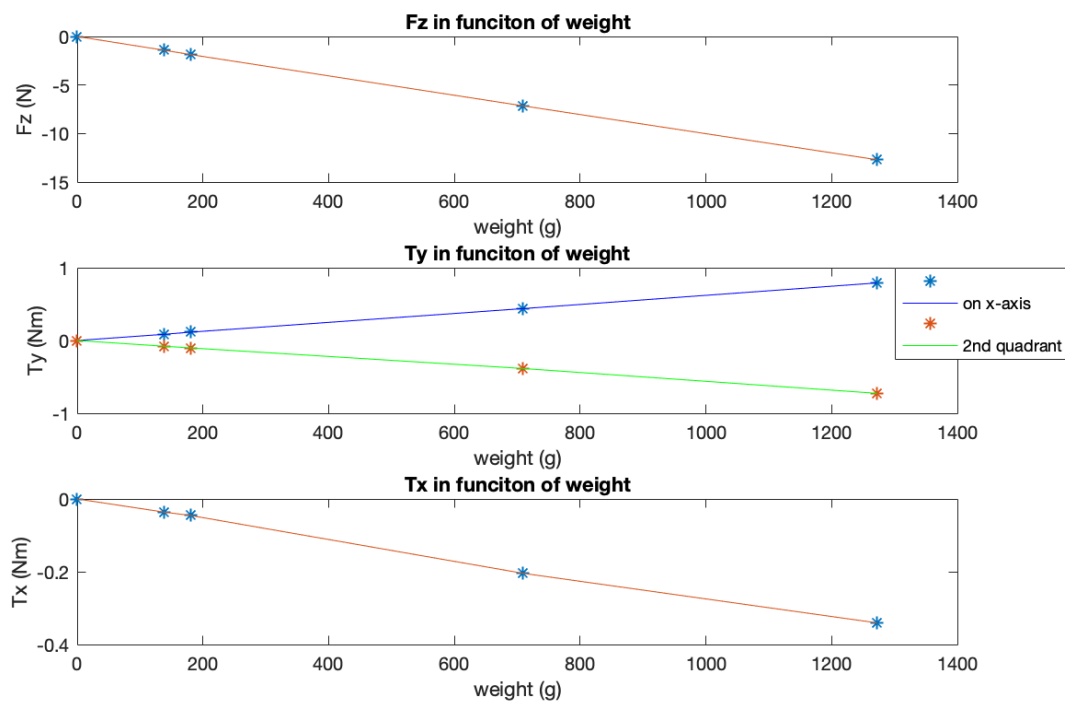


Figure 4.35: Behaviour of F_z , T_y and T_x with increasing load.

Finally, with the measured torques and forces, the location where the surgeon is applying force can be calculated. We assume that all forces are applied on a plane parallel to the xy-plane at a z-coordinate equal to the height of the defect. With this in mind, the aim is to find the x and y coordinates of the tip of the instrument in this plane. Equations 4.31 to 4.34 show how these coordinates are calculated. The variable dz is the thickness of the defect and the bottom clamp and is equal to 16 cm. The variable dx is the distance from the center to the location of the load along the x-axis and dy the distance from the center to the location of the load along the y-axis.

So, (dx,dy) are the coordinates of where the load is applied. When the load is mainly along the xy -plane, like it's the case during suturing, next to the torques induced around the x and y -axis, a torque is also and mainly induced around the z -axis. So, with the distances found with equations 4.32 and 4.34, we can calculate the torque around the z -axis with equation 4.35. This value is then compared with the T_z torque received by the sensor.

$$T_y = -F_z \cdot dx + F_x \cdot dz \quad (4.31)$$

$$\text{So, } dx = -\frac{T_y - F_x \cdot dz}{F_z} \quad (4.32)$$

$$T_x = F_z \cdot dy - F_y \cdot dz \quad (4.33)$$

$$\text{So, } dy = \frac{T_x + F_y \cdot dz}{F_z} \quad (4.34)$$

$$T_z = F_y \cdot dx - F_x \cdot dy \quad (4.35)$$

Chapter 5

Testing and validation

5.1 Validation of the synthetic model

As shown in figure 5.1, a medical expert of the UZ Leuven performed a test surgery on our low fidelity model. The aim of this test surgery was to judge the feasibility of our synthetic model as a surgical trainer.

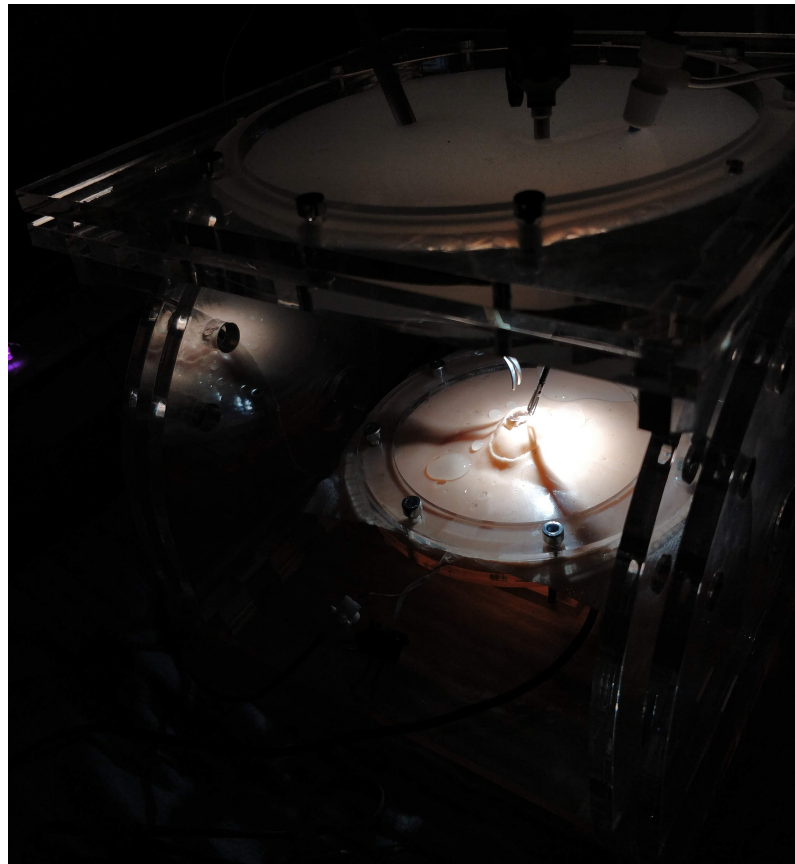


Figure 5.1: A photo taking during the test surgery.

5.1.1 Removable defect

The main focus of the aforementioned test surgery was the removable defect and its ability to simulate the main steps of the surgery. Additionally, the resemblance with the actual defect was assessed.

- Step 1: cutting out the placode. A first remark was that the Ecoflex™ is more slippery than organic tissue, which made it difficult to grab. Secondly, this layer was a little bit too thick to easily puncture but once the cyst was perforated, the cutting went quite easily. The leaking of the fluid from the cyst was said to be realistic. This first step lasted for 6 minutes and 18 seconds. The result after cutting all around the placode can be seen on figure 5.2.

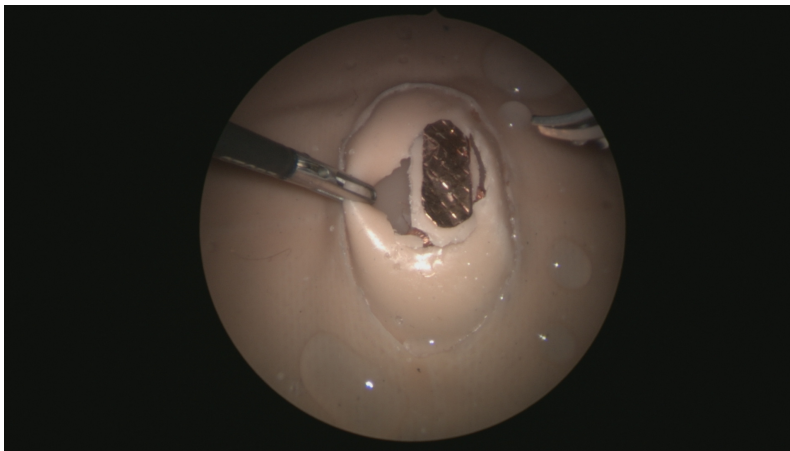


Figure 5.2: Sight of the defect after cutting out the placode.

- Step 2: removal of the excess zona epitheliosa which revealed the underlying nerves. This was considered close to reality and can be seen on figure 5.3. This step was done in 2 minutes and 36 seconds.



Figure 5.3: Sight of the defect after removal of the zona epitheliosa during the test surgery.

- Step 3: undermining the skin radially. The movements needed to separate the two layers radially are similar to the real ones and can be seen on figure 5.4. This step took 17 minutes and 43 seconds.

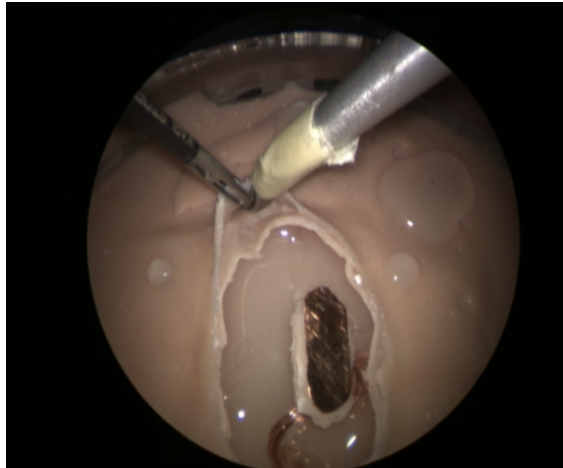


Figure 5.4: Sight of the defect during undermining.

- Step 4: Suturing of both layers. The tension on the mesh embedded Ecoflex™ was too high, which led to tearing. This is shown on figure 5.5. The suturing trials lasted for 20 minutes and 22 seconds.



Figure 5.5: Sight of the defect after removal of the zona epitheliosa during the test surgery.

5.1.2 Uterine environment

While the main focus of the test surgery was to validate the quality of the removable defect, we validated the quality of the uterine environment by requesting feedback from our medical expert and by observing him during the fetoscopic procedure.

5.2 Validation of the sensing system

5.2.1 Connectivity

We created a test setup using a breadboard, the arduino uno, the defect and the grounded scissor instrument. The electrical network of figure 4.10 was reproduced with the defect placed between R_1 and R_3 . A LED is placed in the circuit in series with the grounded instrument to give an indication of when the placode or nerves are touched with the scissor blades. The light goes off as soon as any nervous tissue is touched and glows back when contact is broken. Figure 5.6 shows the circuit with the LED and the defect.

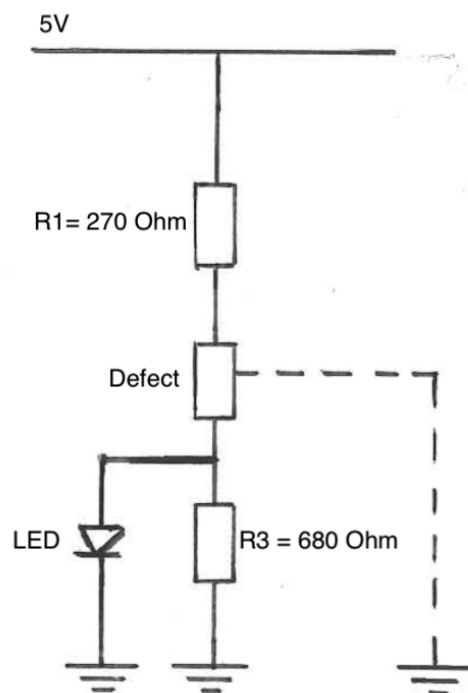


Figure 5.6: Electrical network of the test setup.

The Arduino is programmed to count the number of times the placode or the nerves are touched. The last 15 bits and the current incoming bit are stored in an int variable. A "1" or HIGH signal means no contact whereas a "0" or LOW signal means that the instrument touched the copper wires or foil. If the current bit and the previous one are both "0" and the 4 bits before that are "1", then a contact is sensed and the counter will be increased by one. Two consecutive LOW signals are needed because when there's only one, it will most likely be a mistake. Even if there is an actual contact, it will be too light to harm the placode since a human motion can not go that quickly. For the same purpose of avoiding mistakes, four consecutive HIGH signals are needed between different contacts. When the instrument is in contact with the placode for a longer time, because

of the small movements of the hand, the sensor counts multiple contacts. This is because the placode is not completely flat and contact is broken for a few milliseconds. This problem is tackled by increasing the number of "1" bits required between two different contacts. On the other hand, increasing this number also means that two quick consecutive contacts will only be counted as one touch. We determined empirically that the best balance between these conflicting behaviours was found when four bits were needed between two consecutive contacts.

The same setup as aforementioned was used during the test surgery carried out by the surgeon of the UZ Leuven. So, the surgeon used the grounded scissor instrument during step 1 to 3. The number of times the scissors touched the placode or nerves was recorded and is equal to 90. Twelve of those contacts were intentional and controlled in order to move the placode slightly so they are not harmful. These were announced by the surgeon during the surgery.

5.2.2 Forces on the uterine wall

In section 4.2.2, we created a numerical simulation of the synthetic uterine wall of our model with the onset of being able to compute the forces exerted on it because of instrument motion. As mentioned at the end of section 4.2.2.4, the numerical simulation was not completed in full. However, to validate the algorithms that lead up to this, we completed two experiments discussed below.

5.2.2.1 Instrument motion

In section 4.2.2.2, we designed an algorithm to turn position and orientation tracking from the Aurora system into instrument motion. To prove this algorithm works as intended, we used the position tracking setup shown in figure 4.11 and asked a participant to tilt the instrument in several directions. In figure 5.7, the results of this validation experiment are shown. The participant was first asked to tilt the instrument towards the left and subsequently to tilt it upwards. The simulated versions of these motions are shown in figure 5.7b and 5.7d, respectively.

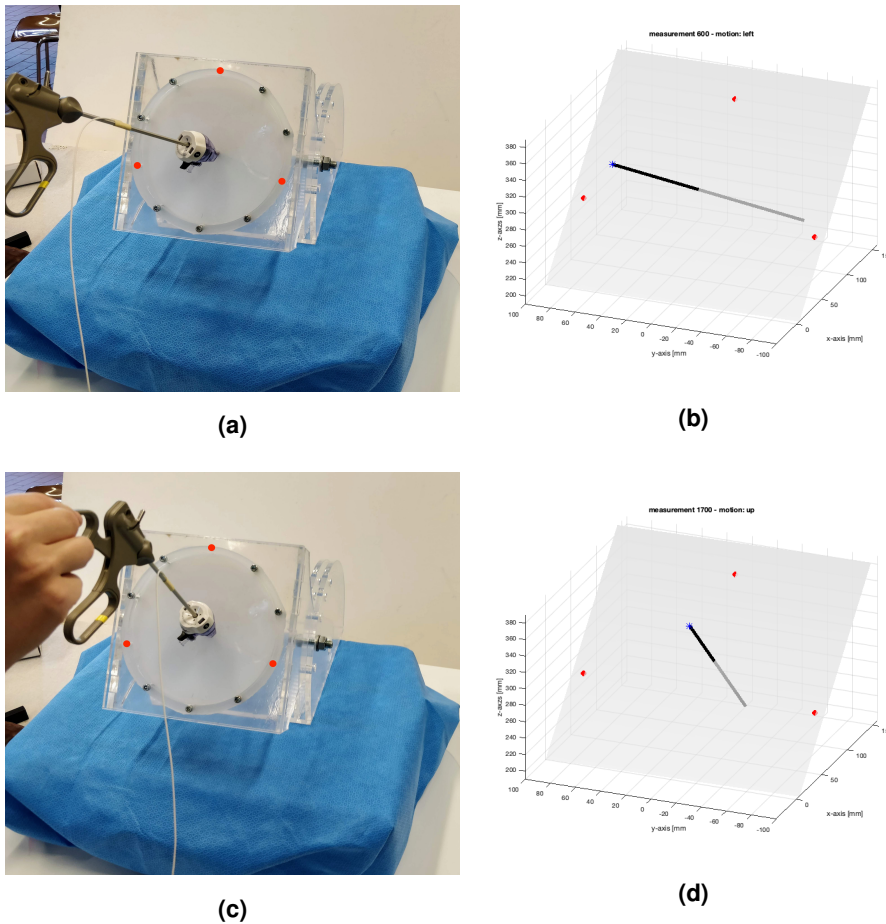


Figure 5.7: A side-by-side comparison showcasing the algorithm which is able to turn position and orientation measurements of an instrument's handle into motion of the entire instrument.

5.2.2.2 Incision port motion

In section 4.2.2.4, we designed an algorithm to turn instrument motion into the motion of the instrument's incision port. To prove this algorithm works as intended, we used the same setup mentioned in section 5.2.2.1. In this experiment, we asked a participant to translate the instrument in a given sequence of directions. In figure 5.8, the results of this validation experiment are shown. The participant was asked to move the instrument to the left of which the trajectory is shown in blue. Next, she was asked to move it to the right (yellow), back to the middle and up (green), down (red) and back up to the middle (magenta).

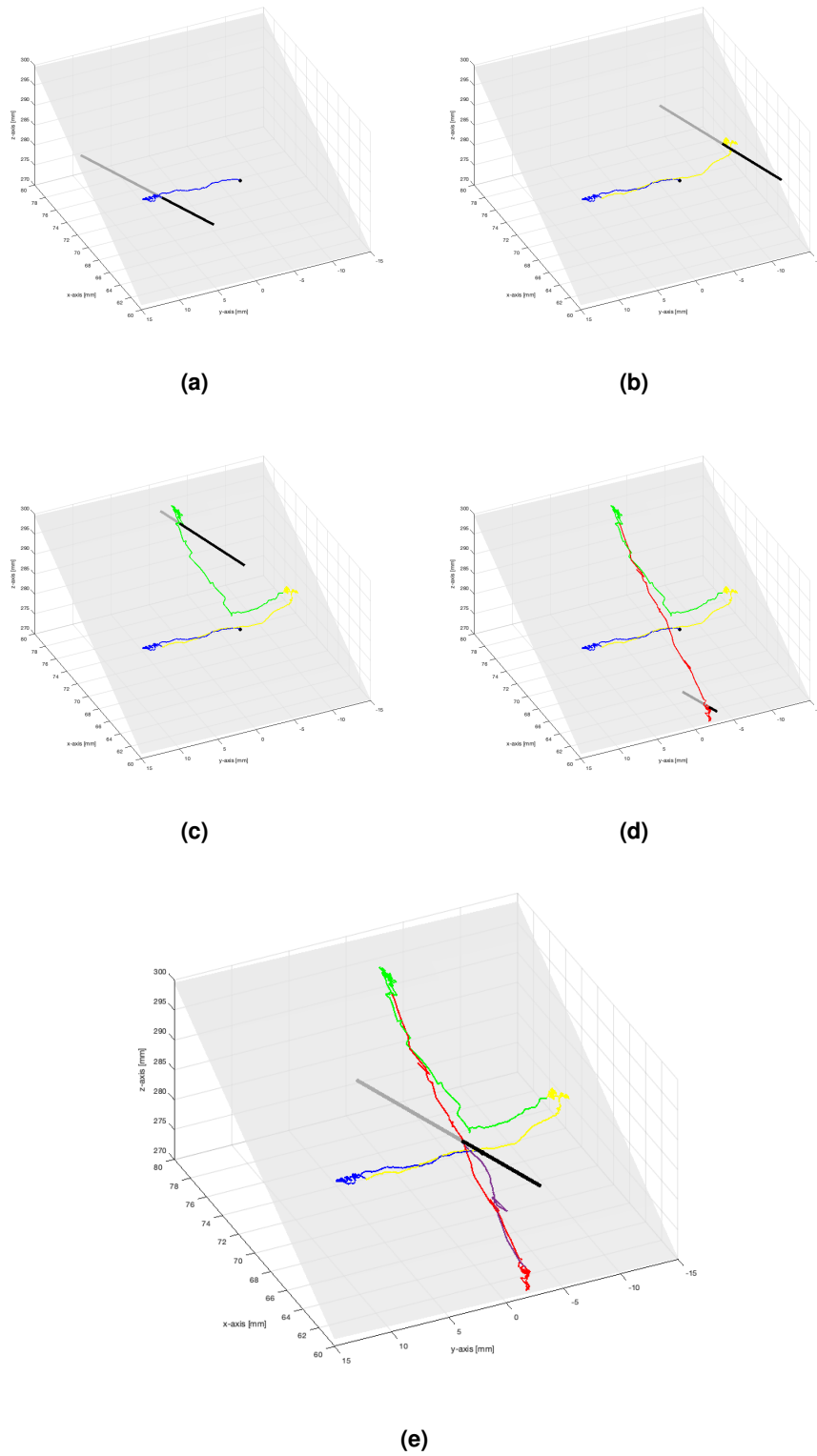


Figure 5.8: A sequence of plots showing the incision port motion due to translational motion of a surgical instrument. The surgical instrument is shown in the figure as the thick black line.

5.2.3 Forces on the fetus

To verify that we are able to find the correct location of the force with the forces and torques coming from the sensor, we use the same setup as in section 4.2.3. We put several known weights on some screws of which we know the exact location. There are seven screws on a circle with diameter 12,5 cm with equal spacing between them. First, the weights (138 g, 180 g, 709 g and 1272 g) are put on the screw situated on the positive x-axis. The exact location is (0,0625; 0) and the average location found by computing the data of the sensor is (0,0588;0,0004). So in the x-direction, the average fault is smaller than 4 mm and less than 0.5 mm in the y direction. Next, the same weights are put three screws further counterclockwise. This is at an angle $154,29^\circ (\frac{360}{7} \cdot 3)$ from the positive x-axis and a radius of 0,0625 m from the centre. The Cartesian coordinates calculated with equations 4.32 and 4.34 from the data of the sensor are changed into Polar coordinates to be able to compare them with the real location. The average radius found is 0,06 m and the average angles is equal to $154,54^\circ$. So the average error on the radius is 2,5 mm and the average angle error is smaller than 1° .

During the feasibility test, the forces and torques that occurred during the surgery were recorded. We were able to compute the data from the surgery to get the locations of the applied forces. During the surgery, the model was placed with the y-axis pointing to the surgeon and the x-axis pointing to his left. This means the the upper parts of the graphs are the closest to the surgeon. The graph on figure 5.9 shows the locations of the forces applied during the first three steps of the surgery, explained in section 5.1.1. During these steps, the main task is cutting, which causes mainly vertical forces. To compute this data, we didn't take the horizontal forces into account since they caused large errors on the location. Also, vertical forces with an absolute value smaller than 1,4 N are not taken into account. When the vertical force is lower than 1,4 N, the relative error due to noise is too high leading to inconsistent outcomes. This threshold was determined iteratively by looking at the locations obtained. So, figure 5.9 shows only the locations of the largest pushing and pulling forces. As expected, most of the forces are applied close to the defect.

Figure 5.10 shows the locations of the forces during the suturing attempts. Here the threshold for F_z is taken much lower (0,9 N) since it's not the main force during suturing. The high horizontal forces will compensate the errors on F_z due to noise. We see that the most forces are applied on the surgeon's left side of the defect, which is also the side were the mesh and Ecoflex™ teared the most.

These results are promising but the algorithm needs to be improved by comparing the results of several surgeries and more extensive testing.

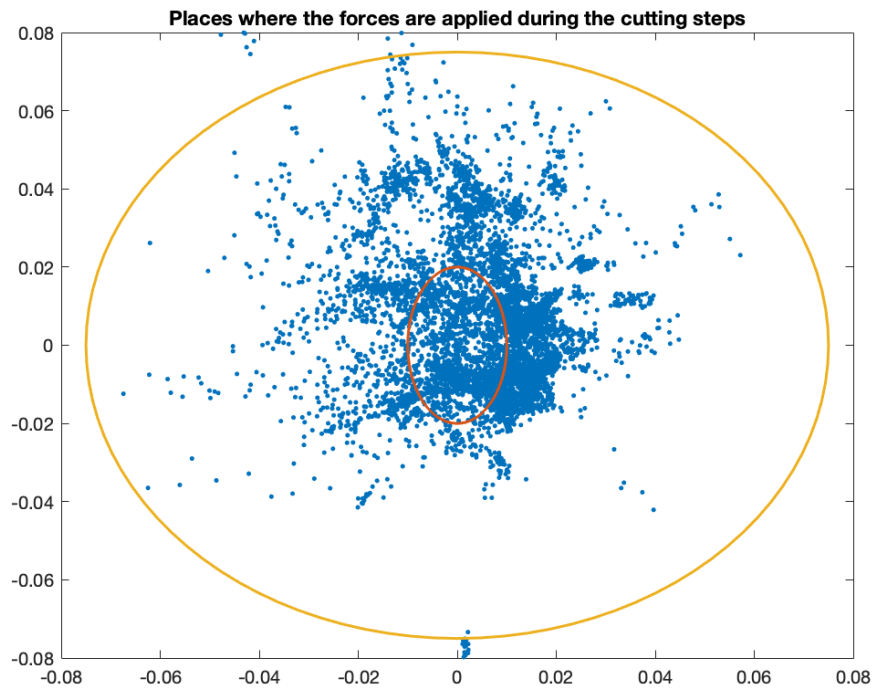


Figure 5.9: Location of the forces during the cutting steps.

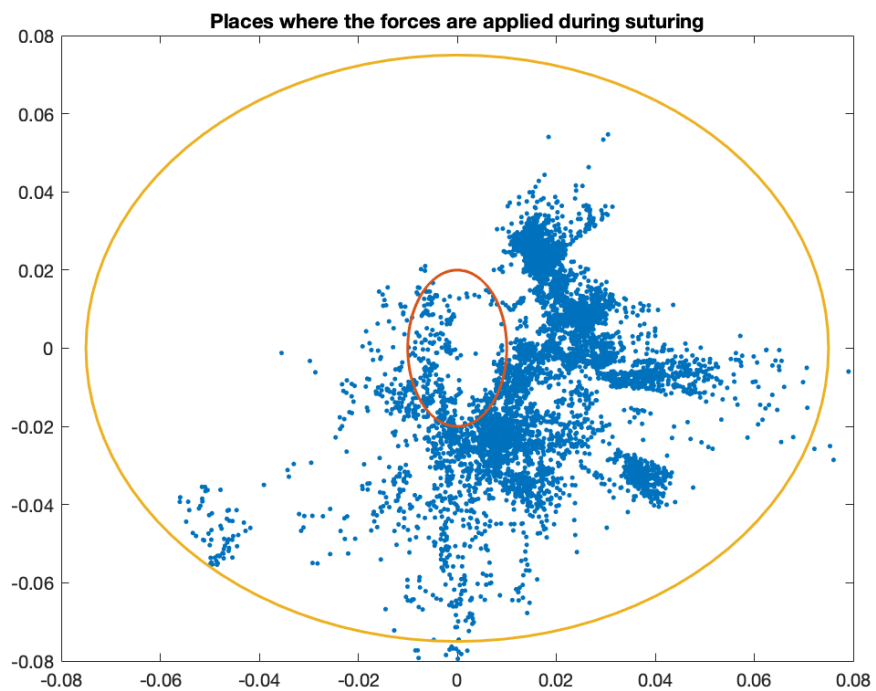


Figure 5.10: Location of the forces during suturing

Chapter 6

Future work

6.1 Synthetic model

The synthetic defect can be improved by preventing it from tearing during suturing. Several methods can be tested to achieve this. The first option is to embed mesh only in a smaller circle in the centre of the defect. Leaving an edge of pure Ecoflex™ near the attaching points would increase the elasticity in all direction. The second alternative is to leave folds of mesh embedded Ecoflex™ left and right at 2 cm of the defect site. This makes sure that, when the surgeon pulls on the Ecoflex™ in the suturing steps, this excess material unfolds. Because of this excess length of material, the tensile stress inside the mesh should not rise as in the test surgery and it should be adequately strong to hold the sutures. A final option is to simply make relieving cuts next to the defect site. These cuts can stretch in the direction with the highest tension thereby transferring some tension in the perpendicular direction.

The defect can also be improved by making the cyst membrane thinner, to make it easier to grasp. A possibility is to remove the mesh at that place and cure it in a flat mold. A elliptical shape of 2x4 mm would have to be cut out of the mesh. Then, a really thin layer of Ecoflex™ is poured evenly on the whole surface. When attaching this layer to the layer underneath, attention must be paid to not attach the unmeshed ellipse. The cyst will then be created by injecting the water in the centre. Only the unmeshed ellipse will rise since it has a high elasticity.

The uterine model can be improved as well by allowing the height of the defect to be slightly adjustable. While the distance requirement was met, it became clear that this could be an additional nice-to-have.

Finally, to be scientifically accepted, the model needs to be validated. To achieve that, an extensive survey needs to be drafted and sent to medical experts. By computing their responses statistically, the quality of the model can be validated.

6.2 Sensing system

In section 4.2.2, we created a numerical simulation of the synthetic uterine wall of our model with the onset of being able to compute the forces exerted on it due to surgical instrument motion. As mentioned before, the numerical simulation was not completed in full. To finish the solver algorithm of the spring model representation of the synthetic uterine wall, an optimization algorithm must be created that minimizes the error value of the position computed in (4.22) by iteratively making new guesses for \mathbf{F}_{ext} . Acceptable termination conditions for the optimization algorithm could involve that the value of (4.22) reaches a certain threshold, indicating that an adequate solution has been found for the node positions. This threshold value for the error could, for example, be 1,20 mm. This is the position accuracy of the 6-DOF Aurora sensors when used in combination with the Aurora PFG (Northern Digital Inc. (2011)).

To calibrate the spring model correctly, the instrument calibrated in section 4.2.2.7 can be used. However, when using it to take measurements to calibrate the spring model, we advise to constrain the motions of the operator to minimize involuntary motions. This can be achieved by, for example, utilizing a mechanical frame that guides the operator performing his movements when performing the calibration experiment.

What became clear during additional measurements performed with the force sensitive instrument is that several measurement spikes were measured while in motion as opposed to holding the instrument in the desired position. Further research can be completed to determine whether this can be addressed to measurement noise, inertial forces or other influences.

In section 4.2.3, we integrated a 6-DOF force sensor to measure the forces exerted on the removable defect. The algorithm that calculates the locations of the forces needs to be improved by comparing the data of several surgeries. An optimization algorithm has to be created to filter out the data that is affected too much by noise. Figures 5.9 and 5.10 can be improved by creating a heat map that shows the locations where the forces have been applied and what the magnitude is at each location. Additionally, to be able to compare several surgeries, a scoring algorithm can be created. To achieve this, a grading system has to be built. One approach is to assign different weights and/or thresholds to the different force and torque directions and to assign higher penalties when exerting force on more sensitive areas of the defect.

Chapter 7

Conclusion

7.1 Synthetic model

The requirements of the synthetic model were based on the most complex steps of the surgery for fetoscopic MMC repair. These requirements were split up and assigned to two different parts; a detailed removable defect and a rudimentary uterine environment. The synthetic model was validated in a feasibility test, in which a medical expert at the UZ Leuven performed the steps of the fetoscopic MMC repair on our model.

7.1.1 Removable defect

The requirements of the removable defect were based on the steps of the surgery that involved the dissection and closing of the MMC defect. These requirements are listed in table 7.1.

Requirements	priority
As cheap as possible	High
Multiple layers	High
Suturable without tearing	High
Defect size: 4 x 2 cm	High
Separable layers at a radius of 2 cm around the defect	High
Modelled nerves	High
Presence of a cyst	Medium
Distinguishable placode	Medium
Cyst filled with liquid	Low

Table 7.1 List of requirements for the removable defect site. This is a copy of table 3.2.

We iteratively designed a defect based on feedback from our medical expert at UZ Leuven and standardized its production process. We iteratively designed a defect based on feedback from our medical expert at UZ Leuven and standardized its production process. Our defect satisfies

- the requirement to be as cheap as possible. The material cost for producing one piece is €3,38.
- the requirement to feature multiple layers. The defect contains a layer of skin and dura, corresponding with the anatomy of the defect.
- the requirement that the incorporated layers should be separable. The quality of the separation is deemed to be close to reality.
- the size requirements of the defect. The actual defect has an elliptical shape of 4x2cm and the available surface for undermining is a circle with a diameter of 13,5 cm.
- the requirement to incorporate a representation of the spinal nerves into the defect.
- the requirement to include a distinguishable placode.
- the requirement to include a cyst in the defect. This cyst can be filled with liquid, simulating the presence of CSF. The leakage of the CSF when the cyst is breached is deemed close to reality.

The only requirement our defect did not satisfy is suturability. A couple of minutes into the closing of the defect, the layers started to tear. Because of this the layers were deemed to be too rigid. We have proposed solutions for this in section 6.2.

7.1.2 Uterine environment

The requirements of the uterine environment were for it to

- feature a distance between 10 and 15 cm from the incision ports to the defect.
- provide the surgeon a similar working area on the outside of the uterine model.
- provide the ability to install new incision ports in every intervention, in any configuration desired.

Based on the feedback received and the observations made during the test surgery, we can make a couple of conclusions about the uterine environment. First, the distance to the defect requirement has been fulfilled by the length of the pivoting arm. Secondly, the working area on the outside of the uterine model proved to be sufficient, the surgeon did not appear to experience any abnormal constraints to his movements because of the uterine wall clamp. Finally, the ability to install new ports in every procedure was achieved by making the synthetic uterine wall removable. In the feasibility test, the port configuration was freely chosen by our medical expert. Additionally, the different tilt configurations of the pivoting arms can be used to select different approach angles for the surgery. This was not validated as only the upright position was used in the feasibility test, but the ability to do so is considered a nice-to-have.

The only considerable point of improvement was that future iterations of the model could incorporate a synthetic uterine wall with an embedded mesh, like the one used in the removable defect.

7.2 Sensing system

7.2.1 Connectivity

The electronic circuit designed to measure connectivity between a surgical instrument and the spinal cord and placode of the defect behaves as designed. However, when analyzing the performance data in the future, it might be useful to be able to make the distinction between intentional and unintentional touching of the placode. As we observed in the feasibility test, the surgeon will tend to gently touch the placode to let it lower into the surrounding cavity created after dissecting the zona epitheliosa.

7.2.2 Forces on uterine wall

The requirement for this part of the sensing system was to be able to estimate the forces exerted on the synthetic uterine wall by the movement of the fetoscopic instruments and to compute the deformation caused by these forces. We created an algorithm that was capable of transforming the instrument motion into the motion of the corresponding incision ports. Next, we discretized the uterine wall into a spring model, but the solver algorithm to compute the correct forces and deformation was only partially completed.

The completed portions of this part were validated by performing two experiments, indicating that it can be used to correctly process the data captured by the Aurora system. The spring model solver algorithm still has to be finished and calibrated. We gave our ideas on how to achieve this in section 6.2.

7.2.3 Forces on fetus

The requirements of this part of the sensing system was to be able to measure the forces exerted on the removable defect and to compute the location at which these forces were applied. We integrated an existing 6-DOF force sensor into our synthetic model and created an algorithm to compute the locations at which the forces were applied on the removable defect from the applied torques.

This integrated setup and algorithm were validated by applying known forces to known positions on the defect. The mean error on the measured vertical forces compared to applied forces is equal to 0,23 N and the locations of where those forces are applied can be determined with an accuracy of 4 mm. However, the algorithm has to be improved for more complex loads.

Bibliography

- Adzick, N. S., Thom, E. A., Spong, C. Y., Brock, J. W., Burrows, P. K., Johnson, M. P., Howell, L. J., Farrell, J. A., Dabrowiak, M. E., Sutton, L. N., Gupta, N., Tulipan, N. B., D'Alton, M. E., and Farmer, D. L. (2011). A Randomized Trial of Prenatal versus Postnatal Repair of Myelomeningocele. *New England Journal of Medicine*, 364(11):993–1004.
- Aggarwal, R., Moorthy, K., and Darzi, A. (2004). Laparoscopic skills training and assessment. *British Journal of Surgery*, 91(12):1549–1558.
- Akoury, H. and Sherman, C. (2008). Uterine Wall Partial Thickness Necrosis Following Combined B-Lynch and Cho Square Sutures for the Treatment of Primary Postpartum Hemorrhage.
- Bauman, J. A., Schwartz, D. M., Welch, W. C., and Sutton, L. N. (2016). Congenital anomalies of the spinal cord.
- Beck, V., Lewi, P., Gucciardo, L., and Devlieger, R. (2012). Preterm prelabor rupture of membranes and fetal survival after minimally invasive fetal surgery: A systematic review of the literature. *Fetal Diagnosis and Therapy*, 31(1):1–9.
- Belfort, M. A., Whitehead, W. E., Bednov, A., and Shamshirsaz, A. A. (2018). Low-Fidelity Simulator for the Standardized Training of Fetoscopic Meningomyelocele Repair. *Obstetrics and gynecology*, 131(1):125–129.
- Bhandari, S., Ganguly, I., Agarwal, P., Singh, A., and Gupta, N. (2016). Effect of myomectomy on endometrial cavity: A prospective study of 51 cases.
- Bibin, L., Anquez, J., Angelini, E., and Bloch, I. (2010). Hybrid 3D pregnant woman and fetus modeling from medical imaging for dosimetry studies. *International Journal of Computer Assisted Radiology and Surgery*, 5(1):49–56.
- Burrows, P. K., Johnson, M. P., Howell, L. J., Farrell, J. A., Dabrowiak, M. E., Sutton, L. N., Gupta, N., Ph, D., Tulipan, N. B., Alton, M. E. D., Farmer, D. L., and Investigators, M. (2011). new england journal. pages 993–1004.
- Cai, C. and Jerry Oakes, W. (2006). Hindbrain herniation syndromes: The Chiari malformations (I and II). *Seminars in Pediatric Neurology*, 4(3):179–191.

- Chmarra, M. K., Bakker, N. H., Grimbergen, C. a., and Dankelman, J. (2007). Optical mouse. (1):38–41.
- Copp, A. J., Stanier, P., and Greene, N. D. E. (2013). Neural tube defects : recent advances , unsolved questions , and controversies. *The Lancet Neurology*, 12(8):799–810.
- Danzer, E., Gerdes, M., Bebbington, M. W., Sutton, L. N., Melchionni, J., Adzick, N. S., Wilson, R. D., and Johnson, M. P. (2009). Lower Extremity Neuromotor Function and Short-Term Ambulatory Potential following in utero Myelomeningocele Surgery. pages 47–53.
- Derossis, A. M., Bothwell, J., Sigman, H. H., and Fried, G. M. (1998). The effect of practice on performance in a laparoscopic simulator. *Surgical Endoscopy*, 12(9):1117–1120.
- Dickson, R. A., Butt, W. P., Dickson, R. A., and Butt, W. P. (2009). Anatomy of the Spine. *The Medico-Legal Back: An Illustrated Guide*, pages 7–36.
- Foley, J. D., van Dam, A., Hughes, J. F., and Feiner, S. K. (1990). *Computer Graphics: principle and practice*. Reading (Massachusetts): Addison-Wesley, 2nd ed. edition.
- Foster, M. R. and Goldstein, J. A. (2017). Surgery for Spina Bifida. pages 1–7.
- Goldberg, A. M., Zurlo, J., and Rudacille, D. (1996). The three Rs and biomedical research. *Science*, 272(5267):1403.
- Gupta, N. and Ross, M. E. (2017). Disorders of Neural Tube Development. In *Swaiman's Pediatric Neurology*, pages 183–191. Elsevier.
- Gupta, P., Kumar, A., and Kumar, A. (2013). Congenital Spinal Cord Anomalies : A Pictorial Review. *YMDR*, 42(2):57–66.
- Heuer, G. G., Scott, N., and Sutton, N. (2014). Fetal Myelomeningocele Closure :. 19104:166–171.
- Hilliard, N. J., Hawkes, R., Patterson, A. J., Graves, M. J., Priest, A. N., Hunter, S., Lees, C., Set, P. A., and Lomas, D. J. (2016). Amniotic fluid volume: Rapid MR-based assessment at 28-32 weeks gestation. *European Radiology*, 26(10):3752–3759.
- Javaux, A., Bouget, D., Gruijthuijsen, C., Stoyanov, D., Vercauteren, T., Ourselin, S., Deprest, J., Denis, K., and Vander Poorten, E. (2018). A mixed-reality surgical trainer with comprehensive sensing for fetal laser minimally invasive surgery. *International Journal of Computer Assisted Radiology and Surgery*, 13(12):1949–1957.
- Javaux, A., Denhaen, M., Hagenimana, Y., Devreker, A., Gruijthuijsen, C., Vercauteren, T., Ourselin, S., Stoyanov, D., Deprest, J., Denis, K., Reynaerts, D., and Vander Poorten, E. (2016). Estimating the interaction forces on the body wall during minimal invasive fetal surgery. *Proceedings of the 6th Joint Workshop on New Technologies for Computer/Robot Assisted Surgery*, pages 110–111.

- Javaux, A., Esteveny, L., Bouget, D., Gruijthuisen, C., Stoyanov, D., Vercauteren, T., Ourselin, S., Reynaerts, D., Denis, K., Deprest, J., and Poorten, E. V. (2017). Body wall force sensor for simulated minimally invasive surgery: Application to fetal surgery. *IEEE International Conference on Intelligent Robots and Systems*, 2017-Sept(July):145–152.
- Jiang, W., Li, G., and Lin, L. (2007). Uterine electromyogram topography to represent synchronization of uterine contractions. pages 120–124.
- Joyeux, L., Danzer, E., Flake, A. W., and Deprest, J. (2018). Fetal surgery for spina bifida. *Archives of Disease in Childhood - Fetal and Neonatal Edition*, 10(1136):1–7.
- Kim, S., Choi, J., Choi, B., and Lee, J. (2015). Hyperelastically stretchable strain gauges based on liquid metals and platinum-catalyzed silicone elastomers. *2015 Transducers - 2015 18th International Conference on Solid-State Sensors, Actuators and Microsystems, TRANSDUCERS 2015*, (c):1093–1096.
- Kohl, T. (2014). Percutaneous minimally invasive fetoscopic surgery for spina bifida aperta. Part I: Surgical technique and perioperative outcome. *Ultrasound in Obstetrics and Gynecology*, 44(5):515–524.
- Lloyd, B. A., Székely, G., and Harders, M. (2007). Identification of spring parameters for deformable object simulation. *IEEE Transactions on Visualization and Computer Graphics*, 13(5):1081–1093.
- Magann, E. F. and Martin J.N., J. (1999). Amniotic fluid volume assessment in singleton and twin pregnancies. *Obstetrics and Gynecology Clinics of North America*, 26(4):579–593.
- Marieb, E. N., Smith, L. A., Mitchell, S. J., and Zao, P. Z. (2015). *Human anatomy & physiology laboratory manual. Cat version*. Pearson, 12th editi edition.
- Menguc, Y. and Wood, R. J. (2014). Characterizing an elastomeric strain sensor at large strains and strain rates. *Workshop on Advances on Soft Robotics*, pages 1–3.
- Miller, J. L., Ahn, E. S., Garcia, J. R., Miller, G. T., Satin, A. J., and Baschat, A. A. (2018). Ultrasound-based three-dimensional printed medical model for multispecialty team surgical rehearsal prior to fetoscopic myelomeningocele repair. *Ultrasound in Obstetrics and Gynecology*, 51(6):836–837.
- Mitchell, L. E., Adzick, N. S., Melchionne, J., Pasquariello, P. S., Sutton, L. N., and Whitehead, A. S. (2004). Spina bifida. pages 1885–1895.
- Mizrahi, J., Karni, Z., and Polishuk, W. Z. (1980). Isotropy and anisotropy of uterine muscle during labor contraction. *Journal of Biomechanics*, 13(3):211–218.
- Munz, Y., Kumar, B. D., Moorthy, K., Bann, S., and Darzi, A. (2004). Laparoscopic virtual reality and box trainers: Is one superior to the other? *Surgical Endoscopy and Other Interventional Techniques*, 18(3):485–494.

- Muth, J. T., Vogt, D. M., Truby, R. L., Mengüç, Y., Kolesky, D. B., Wood, R. J., and Lewis, J. A. (2014). Embedded 3D printing of strain sensors within highly stretchable elastomers. *Advanced Materials*, 26(36):6307–6312.
- Northern Digital Inc. (2011). Aurora.
- Overvelde, J. T., Mengüç, Y., Polygerinos, P., Wang, Y., Wang, Z., Walsh, C. J., Wood, R. J., and Bertoldi, K. (2014). Mechanical and electrical numerical analysis of soft liquid-embedded deformation sensors analysis. *Extreme Mechanics Letters*, 1:42–46.
- Pediatrics, N. (2013). Design of a synthetic simulator for pediatric lumbar spine pathologies. 12(August):192–201.
- Peiro, J. L., Fontecha, C. G., Ruano, R., Esteves, M., Fonseca, C., Marotta, M., Haeri, S., and Belfort, M. A. (2013). Single-Access Fetal Endoscopy (SAFE) for myelomeningocele in sheep model I: Amniotic carbon dioxide gas approach. *Surgical Endoscopy*, 27(10):3835–3840.
- Peirs, J., Clijnen, J., Reynaerts, D., Van Brussel, H., Herijgers, P., Corteville, B., and Boone, S. (2004). A micro optical force sensor for force feedback during minimally invasive robotic surgery. *Sensors and Actuators, A: Physical*, 115(2-3 SPEC. ISS.):447–455.
- Persson, P.-o. and Strang, G. (2004). A simple mesh generator in MATLAB. *Society*, 46(2):329–345.
- Puangmali, P., Liu, H., Althoefer, K., and Seneviratne, L. D. (2008). Optical fiber sensor for soft tissue investigation during minimally invasive surgery. *2008 IEEE International Conference on Robotics and Automation*, pages 2934–2939.
- Qiao, B., Chen, G., and Ye, X. (2009). The research of soft tissue deformation based on mass-spring model. *2009 IEEE International Conference on Mechatronics and Automation, ICMA 2009*, pages 4655–4660.
- Seibold, U., Kübler, B., and Hirzinger, G. (2005). Prototype of instrument for minimally invasive surgery with 6-axis force sensing capability. *Proceedings - IEEE International Conference on Robotics and Automation*, 2005(April):496–501.
- Shim, J.-h., Hwang, N.-h., Yoon, E.-s., Dhong, E.-s., Kim, D.-w., and Kim, S.-d. (2016). Closure of Myelomeningocele Defects Using a Limberg Flap or Direct Repair Original Article. pages 0–5.
- Song, R. B., Glass, E. N., and Kent, M. (2016). Spina Bifida, Meningomyelocele, and Meningocele. *Veterinary Clinics of North America - Small Animal Practice*, 46(2):327–345.
- Stabin, M., Watson, E., Cristy, M., Ryman, J., Eckerman, K., Davis, J., Marshall, D., and Gehlen, M. (1995). *Mathematical models and specific absorbed fractions of photon energy in the non-pregnant adult female and at the end of each trimester of pregnancy.*
- Sutton, L. N., Bauman, J. A., and Macyszyn, L. J. (2015). Spinal Dysraphism and Tethered Spinal Cord.

- Uppal, N. and Saldanha, S. (2012). Training model for low-cost suturing for use in developing nations. *British Journal of Oral and Maxillofacial Surgery*, 50(1):2011–2012.
- Van Loocke, M., Lyons, C. G., and Simms, C. K. (2006). A validated model of passive muscle in compression. *Journal of Biomechanics*, 39(16):2999–3009.
- Van Loocke, M., Simms, C. K., and Lyons, C. G. (2009). Viscoelastic properties of passive skeletal muscle in compression-Cyclic behaviour. *Journal of Biomechanics*, 42(8):1038–1048.
- Venkataramana, N. K. (2011). Spinal dysraphism. *Journal of pediatric neurosciences*, 6(Suppl 1):31–40.
- Walsh, C. J. and Wood, R. J. (2014). Design for manufacturability of soft sensors with discretized stiffness gradients. 10(3).
- Wang, L. L. and Bierbrauer, K. S. (2017). Congenital and Hereditary Diseases of the Spinal Cord. *Seminars in Ultrasound, CT, and MRI*, 38(2):105–125.
- Weiss, S., Jaermann, T., Schmid, P., Staempfli, P., Boesiger, P., Niederer, P., Caduff, R., and Bajka, M. (2006). Three-dimensional fiber architecture of the nonpregnant human uterus determined ex vivo using magnetic resonance diffusion tensor imaging. *Anatomical Record - Part A Discoveries in Molecular, Cellular, and Evolutionary Biology*, 288(1):84–90.
- Williams, B. (1981). Chronic herniation of the hindbrain. *Annals of the Royal College of Surgeons of England*, 63(1):9–17.
- Williams, H. (2008). A unifying hypothesis for hydrocephalus, Chiari malformation, syringomyelia, anencephaly and spina bifida. *Cerebrospinal Fluid Research*, 5:1–11.
- Xu, S., Liu, X., and Zhang, H. (2009). Simulation of soft tissue using mass-spring model with simulated annealing optimization. *Proceedings of the 2009 IEEE International Conference on Automation and Logistics, ICAL 2009*, (August):1543–1547.
- Zhang, S., Gu, L., Huang, P., and Xu, J. (2005). Real-Time Simulation of Deformable Soft Tissue Based on Mass-Spring and Medial Representation. pages 419–426.

Appendix A

Technical specifications of Ecoflex™

TECHNICAL OVERVIEW


	Mixed Viscosity (ASTM D-2393)	Specific Gravity (g/cc) (ASTM D-1475)	Specific Volume (cu. in./lb.) (ASTM D-1475)	Pot Life (ASTM D-2471)	Cure Time	Shore Hardness (ASTM D-2240)	Tensile Strength (ASTM D-412)	100% Modulus (ASTM D-412)	Elongation at Break % (ASTM D-412)	Die B Tear Strength (ASTM D-624)	Shrinkage (in./in.) (ASTM D-2566)
Ecoflex™ 5	13,000 cps	1.07	25.8	1 min.	5 min.	5A	350 psi	15 psi	1000%	75 pli	< .001 in./in.
Ecoflex™ 00-50	8,000 cps	1.07	25.9	18 min.	3 hours	00-50	315 psi	12 psi	980%	50 pli	< .001 in./in.
Ecoflex™ 00-30	3,000 cps	1.07	26.0	45 min.	4 hours	00-30	200 psi	10 psi	900%	38 pli	< .001 in./in.
Ecoflex™ 00-33 AF	3,000 cps	1.07	26.0	45 min.	4 hours	00-33	200 psi	10 psi	900%	38 pli	< .001 in./in.
Ecoflex™ 00-20	3,000 cps	1.07	26.0	30 min.	4 hours	00-20	160 psi	8 psi	845%	30 pli	< .001 in./in.
Ecoflex™ 00-10	14,000 cps	1.04	26.6	30 min.	4 hours	00-10	120 psi	8 psi	800%	22 pli	< .001 in./in.

*All values measured after 7 days at 73°F/23°C


Figure A.1: Technical specifications of Ecoflex™

Appendix B

Specifications of Sylamed compresses




Gamme Hospitalière



Compresses en non-tissé non stériles

SylaSoft



Description :
Compresses en non tissé composées de viscose et de polyester conformes à la Pharmacopée européenne et aux normes EDANA 1996, stérilisation possible à l'oxyde d'éthylène, au rayonnement ou à la vapeur - Classe I.

Conditionnement :
Paquet de 100 compresses.

Indication :
Dispositif adapté à tous les soins médicaux: hygiène, déterision, antiseptie, couverture et soins de plaies. Sa structure homogène permet une sensation de douceur au contact de la peau et un faible risque d'effilochage. Il permet le recouvrement non aseptique des plaies.

Référence	Poids - Epaisseurs	Dimensions pliées	Dimensions dépliées	Paquets par carton	Unités par carton
211	30g - 4	5 x 5 cm	10 x 10 cm	50	5 000
213	30g - 4	7,5 x 7,5 cm	15 x 15 cm	50	5 000
217	30g - 4	10 x 10 cm	20 x 20 cm	50	5 000
219	30g - 4	10 x 20 cm	20 x 40 cm	50	5 000
111	40g - 4	5 x 5 cm	10 x 10 cm	50	5 000
113	40g - 4	7,5 x 7,5 cm	15 x 15 cm	50	5 000
115	40g - 4	7,5 x 10 cm	15 x 20 cm	50	5 000
117	40g - 4	10 x 10 cm	20 x 20 cm	50	5 000
119	40g - 4	10 x 20 cm	20 x 40 cm	50	5 000

4

Figure B.1: Specifications of SylaSoft compresses (<http://www.sylamed.com/>)

Appendix C

Technical specifications of Arduino Uno Rev3

Microcontroller	ATmega328P
Operating Voltage	5V
Input Voltage (recommended)	7-12V
Input Voltage (limit)	6-20V
Digital I/O Pins	14 (of which 6 provide PWM output)
PWM Digital I/O Pins	6
Analog Input Pins	6
DC Current per I/O Pin	20 mA
DC Current for 3.3V Pin	50 mA
Flash Memory	32 KB (ATmega328P) of which 0.5 KB used by bootloader
SRAM	2 KB (ATmega328P)
EEPROM	1 KB (ATmega328P)
Clock Speed	16 MHz
LED_BUILTIN	13
Length	68.6 mm
Width	53.4 mm
Weight	25 g

Figure C.1: Technical specifications of Arduino Uno Rev3

Appendix D

Specifications and drawings of the 6-DOF force and torque sensor

Ranges and Resolutions
Specifications
Drawings
Documents

Select a system type. (For more information on system types, please see our [F/T Product Description](#) page.)

16-Bit DAQ, ECAT, Net, TWE or WNet F/T System
 Controller F/T System

Standard Calibrations (US)

Calibration	Fx,Fy	Fz	Tx,Ty	Tz	Fx,Fy	Fz	Tx,Ty	Tz
US-25-25	25 lbf	100 lbf	25 lbf-in	25 lbf-in	1/224 lbf	3/224 lbf	1/160 lbf-in	1/320 lbf-in
US-50-50	50 lbf	200 lbf	50 lbf-in	30 lbf-in	1/112 lbf	3/112 lbf	1/80 lbf-in	1/160 lbf-in
SENSING RANGES				RESOLUTION				

[View Standard \(US\) Complex Loading Graph](#)

Metric Calibrations (SI)

Calibration	Fx,Fy	Fz	Tx,Ty	Tz	Fx,Fy	Fz	Tx,Ty	Tz
SI-125-3	125 N	500 N	3 Nm	3 Nm	1/48 N	1/16 N	1/1320 Nm	1/2640 Nm
SI-250-6	250 N	1000 N	6 Nm	3.4 Nm	1/24 N	1/8 N	1/660 Nm	1/1320 Nm
SENSING RANGES				RESOLUTION				

[View Metric \(SI\) Complex Loading Graph](#)

*The resolution is typical for most applications and can be improved with filtering.
**Resolutions quoted are the effective resolution after dropping four counts of noise.
***Applied loads must be within range in each of the six axes for the F/T sensor to measure correctly.

ATI's F/T calibrations are traceable to the National Institute of Standards and Technology (NIST). ATI certifies sensors are calibrated in accordance with applicable ATI procedures. These procedures are compliant with the ISO 9001 standard to ensure that products are within ATI specifications.

[Contact your sales representative for accuracy information.](#)

Figure D.1

Ranges and Resolutions		Specifications	Drawings	Documents
<input type="radio"/> US (Standard) <input checked="" type="radio"/> SI (Metric)				
Single-Axis Overload				
F _{xy}		±2300 N		
F _z		±7300 N		
T _{xy}		±43 Nm		
T _z		±63 Nm		
Stiffness (Calculated)				
X-axis & Y-axis forces (K _x , K _y)		5.3x10 ⁷ N/m		
Z-axis force (K _z)		1.1x10 ⁸ N/m		
X-axis & Y-axis torque (K _{tx} , K _{ty})		6.5x10 ³ Nm/rad		
Z-axis torque (K _{tz})		9.2x10 ³ Nm/rad		
Resonant Frequency				
F _x , F _y , T _z		3600 Hz		
F _z , T _x , T _y		3800 Hz		
Physical Specifications				
Weight*		0.0634 kg		
Diameter*		25 mm		
Height*		21.6 mm		
* Specifications include standard interface plates.				

Figure D.2

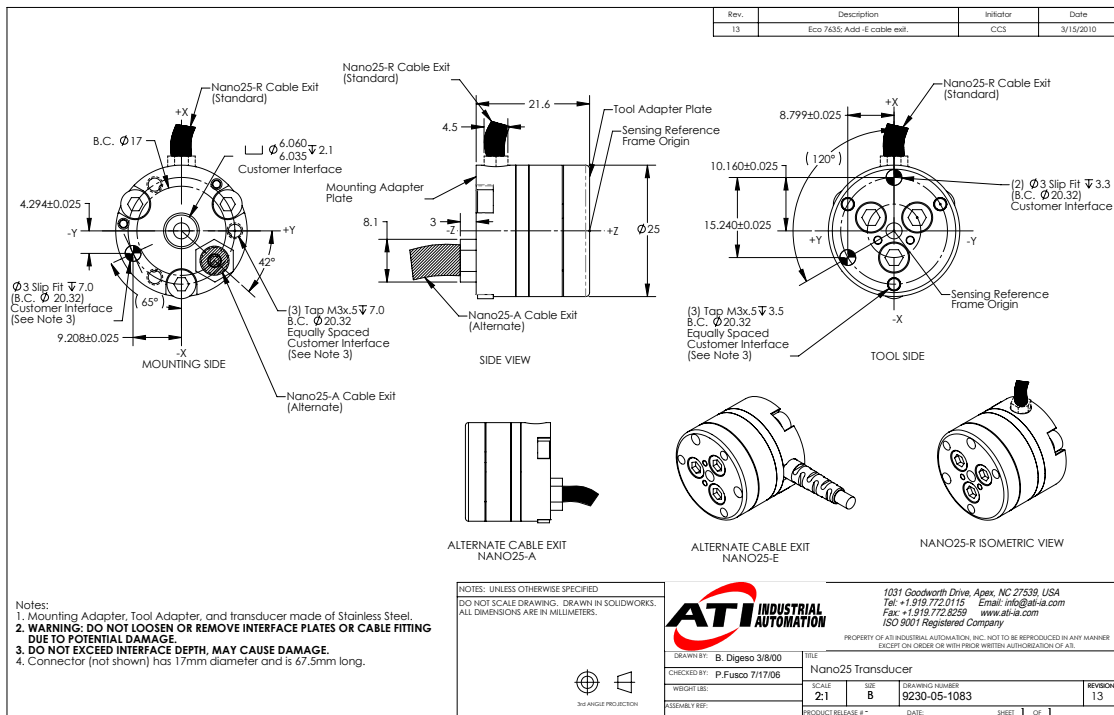


Figure D.3

FACULTEIT INDUSTRIËLE INGENIEURSWETENSCHAPPEN
CAMPUS GROEPT LEUVEN
Andreas Vesaliusstraat 13
3000 LEUVEN, België
tel. + 32 16 30 10 30
iiw.groept@kuleuven.be
www.iw.kuleuven.be

